

Atlas of CO-Line Shells and Cavities around Galactic Supernova Remnants with FUGIN*

YOSHIAKI SOFUE ,¹ MIKITO KOHNO ,² AND TOMOFUMI UMEMOTO ,^{3,4}

¹ Institute of Astronomy, The University of Tokyo, 2-21-1 Mitaka, Tokyo 181-8588, Japan

² Astronomy Section, Nagoya City Science Museum, 2-17-1 Sakae, Naka-ku, Nagoya, Aichi 460-0008, Japan

³ Nobeyama Radio Observatory, National Astronomical Observatory of Japan (NAOJ), National Institutes of Natural Sciences (NINS), 462-2 Nobeyama, Minamimaki, Minamisaku, Nagano 384-1305, Japan

⁴ Department of Astronomical Science, School of Physical Science, SOKENDAI (The Graduate University for Advanced Studies), 2-21-1 Osawa, Mitaka, Tokyo 181-8588, Japan

(Received 2020 October 22; Revised 2020 November 17; Accepted 2020 November 23)

Submitted to ApJS

ABSTRACT

A morphological search for molecular shells and cavities was performed around 63 Galactic supernova remnants (SNR) at $10^\circ \leq l \leq 50^\circ$, $|b| \leq 1^\circ$ using the FUGIN (FOREST Unbiased Galactic Imaging survey with the Nobeyama 45-m telescope) CO line data at high angular ($20''$) and velocity (1.3 km s^{-1}) resolutions. The results are presented as supplementary data for general purpose for investigations of the interaction between SNRs and interstellar matter in the form of an atlas of CO-line maps superposed on radio continuum maps at 20 cm along with a list of their kinematic distances determined from CO-line radial velocities.

Keywords: ISM, Supernova remnants — ISM, molecular cloud — catalogs — surveys

1. INTRODUCTION

The interaction between shock waves of supernova remnants (SNR) and molecular clouds (MC) has been a long-standing issue in the physics of the interstellar medium (ISM) (Chevalier 1977, 1999; Shull 1980; Lucas et al. 2020). The major concerns about the interaction are the generation of interstellar turbulence (Kilpatrick et al. 2016), triggering or suppression of star formation (McKee & Ostriker 1977; Cox et al. 1999; Seta et al. 2004), and cosmic ray acceleration (Fujita et al. 2009; Kuriki et al. 2018; Maxted et al. 2019; Sano et al. 2019).

Extensive observations of association of molecular clouds with well studied SNRs have been obtained in the last decades by molecular line observations (Tatematsu et al. 1990; Koo & Moon 1997; Tian et al. 2007; Ranasinghe & Leahy 2018; Lee et al. 2020). The current 'association' has been discussed mainly by the coincidence of the distance of an SNR measured by some means with the kinematic distance of the cloud from radial velocity, leaving large uncertainty on the order of $\sim 1 \text{ kpc}$. On the other hand, the association based on the morphological shell structure concentric to the SNR's shock front has been obtained in few cases.

In this paper, we perform a systematic search for CO-line shells and/or cavities based on morphological association with the SNRs listed in the Green's catalogue (<http://www.mrao.cam.ac.uk/surveys/snrs>) (Green 2009; Green & Dewdney 1992; Green 2019). We use ^{12}CO and ^{13}CO ($J = 1 - 0$) line channel maps from the FUGIN data set (Minamidani et al. 2016; Umemoto et al. 2017).

The purpose of this paper is to present the result in the form of an atlas of the identified molecular cavities and shells, and to provide with a finding chart for general purpose of the research of the interaction between SNRs and the ISM in the Galactic disc.

2. DATA

Corresponding author: Yoshiaki Sofue
sofue@ioa.s.u-tokyo.ac.jp

* FUGIN: FOREST (FOur beam REceiver System on the 45-m Telescope) Unbiased Galactic plane Imaging with the Nobeyama 45-m telescope

Table 1. Parameters of data sets

Telescope/Survey	Line/Band	Effective Resolution	Velocity Resolution	References
Nobeyama 45-m/FUGIN	^{12}CO $J = 1-0$	20''	1.3 km s $^{-1}$	Umemoto et al. (2017) ¹
	^{13}CO $J = 1-0$	21''	1.3 km s $^{-1}$	Umemoto et al. (2017)
VLA/VGPS	21 cm	$\sim 1'$	—	Stil et al. (2006) ²
VLA/MAGPIS	20 cm	$\sim 6''$	—	Helfand et al. (2006) ³
Effelsberg 100-m/Galactic Plane	21 cm	$\sim 9.4'$	—	Reich et al. (1997) ⁴

[1] <http://nro-fugin.github.io>

[2] http://www.ras.ucalgary.ca/VGPS/VGPS_data.html

[3] <https://third.ucllnl.org/gps/index.html>

[4] <http://www3.mpifr-bonn.mpg.de/survey.html>

Table B lists the SNRs from the Green's catalogue located in the FUGIN survey area at $10^\circ \leq l \leq 50^\circ$ and $|b| \leq 1^\circ$ and $190^\circ \leq l \leq 230^\circ$. Figure 4 shows the positions of the SNRs on the color-coded maps of the peak T_B of the ^{12}CO , ^{13}CO , and C^{18}O line emission in the first Galactic quadrant (Umemoto et al. 2017). In order to compare the distributions of the CO line emission with radio distribution of the SNRs, we extracted 21 cm radio continuum maps of the SNRs from the archival web sites of the Multi-Array Galactic Plane Imaging Survey (MAGPIS: Helfand et al. (2006)), VLA Galactic Plane Survey (VGPS: Stil et al. (2006)), and the Effelsberg radio continuum survey (Reich et al. 1997). We summarize the parameters of data sets in Table 1.

The FUGIN project provided with high-sensitivity, high-spatial and velocity resolution, wide velocity (482 channels \times 0.65 km s $^{-1}$) and wide field ($40^\circ \times 2^\circ$ along the Galactic plane from $l = 10^\circ$ to 50°) coverage by $(l, b, v_{\text{lsr}} : T_B)$ cubes in the ^{12}CO , ^{13}CO and C^{18}O ($J = 1 - 0$) lines. The full beam width at half maximum of the telescope was 15'' at the ^{12}CO ($J = 1 - 0$)-line frequency, and the velocity resolution was 1.3 km s $^{-1}$. The effective beam size of the final data cube was 20'', and the rms noise levels were ~ 1 K. The final 3D FITS cube had a voxel size of $(\Delta l, \Delta b, \Delta v_{\text{lsr}}) = (8.5'', 8.5'', 0.65 \text{ km s}^{-1})$, which are available as the archival data.

3. ATLAS

3.1. Identification

We present the atlas of molecular cavities, shells and partial arcs apparently surrounding the SNRs by superposition of ^{12}CO channel maps on radio continuum maps at 20 cm.

The search for a CO shell associated with a SNR was done by the following procedure. Since the distance of a SNR is unknown, or uncertain even if it exists, so that its radial velocity is not known, the search for the shell structure was done in all the 462 channels of the CO data cube from -100 to 200 km s $^{-1}$ by one channel after another for each SNR.

First we display the radio continuum image on the screen, and superpose a channel map (T_B map) on the same screen. Then, the CO channel is changed from 1st to 462nd step by step. Numerous CO clouds and filaments will pass by, mostly fore- and background emissions, but at a certain velocity channel, a possible shell/cavity/arc appears apparently associated with the SNR's shell edge.

Once such a candidate was found, its nearby channels are inspected more carefully, and the clearest shell feature was chosen as the associated shell, and its channel velocity was adopted as the radial velocity of the shell. This was repeated in ^{12}CO and ^{13}CO cubes, each 462 channels, for all the 63 SNRs. The C^{18}O data were not used for their too low brightness for the present purpose.

Table B in Appendix B lists the Galactic positions (l, b), radial velocities (v_{lsr}), kinematic distances (d), and linear diameters (D) of the candidates cavities and/or shells of the analyzed SNRs. References to molecular-line observations, which report the association of the same or close radial velocities are cited in the last column. Objects without references are mostly new measurements currently with no information about molecular gas association.

The measured results are presented in the form of T_B maps (sometimes I_{CO} maps) in the ^{12}CO line emission of the CO shells, arcs, and/or concentric alignment of clumps, as superposed on 20-cm radio continuum maps, in figures 5

to 51 of Appendix C. We also present superposed ^{13}CO and ^{12}CO maps by R (red) and G (green) color-coded images in order to show the degree of condensation of the molecular gas density.

The association of the SNR and the identified molecular shell/cavity has been obtained purely by morphological inspection into the CO-line channel maps. This means that, despite of coincidence of the concave edge of a CO cloud with the SNR's outer edge, the physical (true) association cannot be proved from the present analysis, which applies to all the SNRs studied in this paper. A direct way to prove the association is their distance coincidence on the line of sight with a sufficiently high accuracy, e.g. within an error of a few tens of pc. However, the kinematical distance from the molecular line includes uncertainty of ~ 1 kpc; distance estimation by SNR's brightness to diameter ($\Sigma - D$) relation yields even larger uncertainty; and the method to measure the radio continuum absorption by an HI cloud includes a problem of the association of the HI and CO clouds themselves.

Thus, the atlas presents only the candidate molecular structures. More advanced discussion about the interaction may be obtained by further, sophisticated observations of a signature of the physical compression by a shock wave such as shock-induced molecular lines (Koo & Moon 1997; Ziurys et al. 1989; Seta et al. 2004; Sashida et al. 2013).

Nevertheless, it may be worthwhile to comment that the here determined radial velocities, hence kinematical distances, of the identified molecular shells for some typical SNRs are in good agreement with those currently reported in the literature such as G11.17-0.35 at $v_{\text{lsr}} = 33 \text{ km s}^{-1}$ (Kilpatrick et al. 2016), and W44 at $40 - 50 \text{ km s}^{-1}$ (Seta et al. 2004), for example. In table B we cite more references, in which the same or close velocity clouds are identified by independent CO line observations.

3.2. Morphological classification

A SNR interacting with a molecular cloud will deform the cloud to make a concave boundary with respect to the SNR center. Thereby, the resulting cloud morphology will depend on the extent and density of the cloud. We categorize the structure of a shell or a cavity of the CO brightness distribution apparently surrounding a SNR as follows:

i) Cavity (Ca κ): When the cloud is extended more largely than the SNR size or comparable, a round cavity is created around the SNR due to dissociation of molecular gas and accumulation at the shock front. If the cloud size is sufficiently large, the cavity will be fully embedded in the cloud, making a round shape on the sky. We define such a case a cavity with completeness of 1 or 100%, and introduce a completeness parameter or the shell measure, $\kappa = 1$. If the cloud size is comparable or smaller, the dissociation and/or compression will take place partially, forming open cavity to the inter-cloud space. Such a partial cavity may be categorized by its completeness or shell measure with $\kappa < 1$, depending on the fraction of the boundary from a perfect loop.

ii) Shell (Sh κ): If the cloud's density is lower, the gas will be accumulated or snow-plowed around the shock front, making a shell structure. The shell may be categorized by its completeness from $\kappa = 1$ showing a perfect loop, or partial loops with $\kappa < 1$.

iii) Partial/clumpy shell (Ps=Cs κ): Clouds are often more turbulent and clumpy. In such a case, the interaction front will produce more partial features such as a clumpy shell or an ensemble of partial arcs. We categorize such a case by the fraction of the total partial arcs compared to a round loop by a factor of κ .

Figure 1 illustrates typical morphologies of the CO brightness distribution around a SNR.

Descriptions of the properties of the obtained maps are given in figure captions of individual objects in the atlas. We here present an example for G11.17-0.35+32.975 km s^{-1} in figure 2. This SNR is a typical bright shell in radio continuum, and its western half is apparently contacting, on the sky, with a half-cavity of a CO line cloud (Kilpatrick et al. 2016). The RGB image indicates that the edge of the cavity facing the SNR does not show a signature of strong compression of gas, which would cause a red-color (^{13}CO) excess, if it existed. Also, the molecular mass (luminosity) along the edge of the cavity is far smaller than that expected by snow-plowed mass from inside the cavity. Such a structure may imply that the shell was created by dissociation of molecules, but not by a direct snow-plowing compression.

3.3. Distances

The radial velocity, $v_r = v_{\text{lsr}}$, at a distance d orbiting around the Galactic Center is related to the circular rotation velocity $V(R)$ as a function of the galacto-centric distance R as

$$v_r = \left(\frac{R_0}{R} V(R) - V_0 \right) \sin l, \quad (1)$$

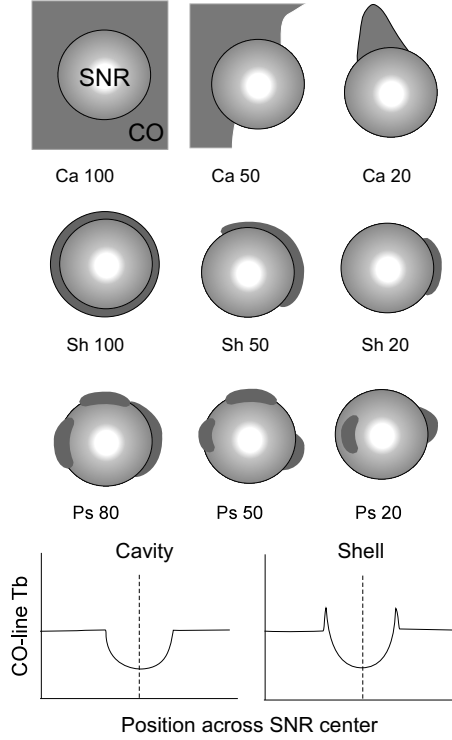


Figure 1. Shell types and shell measure .

where R is the galacto-centric distance related to d and galactic longitude l by

$$d = R_0 \cos l \pm \sqrt{R^2 - R_0^2 \sin^2 l}. \quad (2)$$

We assume here $V_0 = 238 \text{ km s}^{-1}$ and $R_0 = 8.0 \text{ km s}^{-1}$ (Honma et al. 2015), and adopt the most recent rotation curve derived by compilation of determined circular velocities in the last two decades as shown in figure 3 (Sofue 2020). Here, we approximate the rotation curve by an analytic expression,

$$V(R) = \left(\frac{V_1}{[1 + (R/a)^2]^{1/2}} + \frac{V_2}{1 + (R/b)^2} \right) \left(\frac{R}{c} \right). \quad (3)$$

The parameters, $V_1 = 67$, $V_2 = 1000 \text{ km s}^{-1}$, $a = 3.5 \text{ kpc}$, $b = 0.44 \text{ kpc}$, $c = 1 \text{ kpc}$, were determined by iterative fitting of the function to the data by trial and error, until one gets satisfactory reproduction of the data within radius range, 1.4 to $\sim 10 \text{ kpc}$, necessary for the present analysis. The adopted curve is shown by the thick line in figure 3.

For a given set of v_r and l , we can determine R by iteration using equations 1 and 3, and the distance d is obtained by equation 2. In table B we list the determined distances and diameters of the SNR. The errors are calculated using the uncertainty of radial velocity of the CO line in the measured value as well as the interstellar turbulence, $\delta v_{\text{lsr}} \sim 5 \text{ km s}^{-1}$, and the uncertainty in the rotation velocity, $\delta V_{\text{rot}} \sim 5 \text{ km s}^{-1}$, propagating through the above equations to d . The uncertainties in R_0 and V_0 are not included.

3.4. Molecular mass

The molecular mass of associated clouds is one of the most essential quantities. However, the present resolution, $20'' \sim 0.5 \text{ pc}$ at 5 kpc for example, is a few orders of magnitudes wider than the expected thickness of shock-compressed filaments at the SNR fronts (Lucas et al. 2020). So, we are not able to estimate meaningful mass of the directly associated molecular gas to the SNRs.

Instead, we here try to estimate the upper limit to the associated cloud for G11.17-0.35 as a typical example. Measuring the excess T_B at the edge of the SNR over that in the ambient emission outside SNR, the upper limit mass

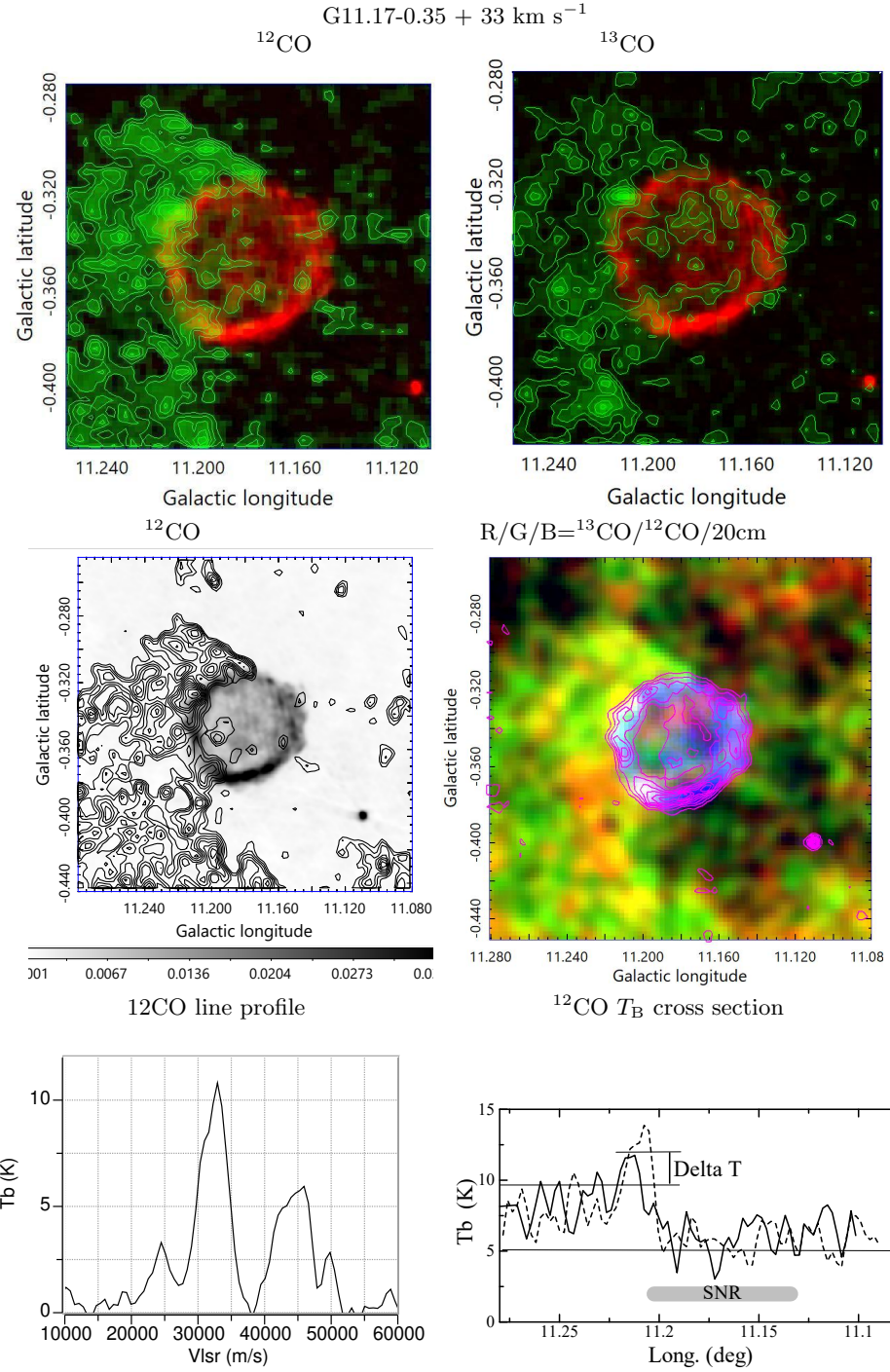


Figure 2. Example of molecular cavity/shell of Ca/Sh 50 toward SNR G11.17-0.35 at $v_{\text{lsr}} = +32.925 \text{ km s}^{-1}$ by (top left) ^{12}CO contours from 7 K every 1 K on 20 cm in red; (top right) ibid, 7 K every 0.5 K, superposed on a grey-scale map of 20 cm radio continuum from 0 to 0.03 Jy beam⁻¹; (middle left) CO from 2 K every 1 K; (middle right) RGB color coded images of ^{13}CO (red: auto), ^{12}CO (green: auto) and 20 cm (blue: auto, magenta contour interval by 5 mJy beam⁻¹); (bottom left) ^{12}CO line spectrum at the western edge; (bottom right) ^{12}CO T_{B} across the SNR center along $b = -0.34^{\circ}$ (dash) and -0.36° (full line), showing the 'cavity' property. All figures of the studied SNRs are presented in the supplementary data described in the text.

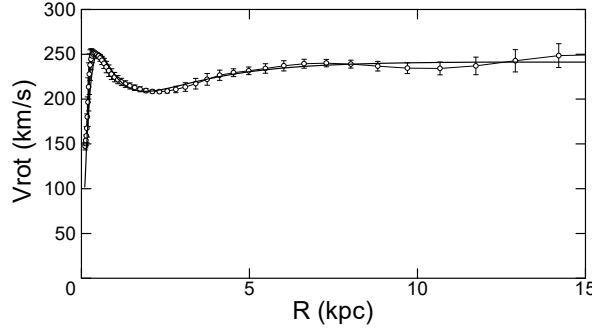


Figure 3. The most recent rotation curve (thin line with circles and standard errors) (Sofue 2020), and the used model rotation curve expressed by equation 3.

may be calculated by

$$M \sim \mu m_H 2\pi\kappa R_s \delta R_{\text{beam}} X_{\text{CO}} \int \delta T dv, \quad (4)$$

where $\mu \sim 2.6$ is the reduced mass per H₂ molecule for solar abundance, m_H is the hydrogen mass, $X_{\text{CO}} \sim 2 \times 10^{20} \text{ cm}^{-2} [\text{K km s}^{-1}]^{-1}$ (Sofue & Kohno 2020) is the conversion factor, R_s is the SNR radius, $\delta R_{\text{beam}} = \theta_{\text{beam}} r$ is the beam width at the object, κ is the cavity/shell measure, and δT is the excess brightness temperature of ¹²CO line at the intensity peak along the shell or the edge of cavity contacting the SNR.

For G11.17-0.35 at 33 km s⁻¹ (figure 2), we obtain $\delta T \sim 5$ K and $\kappa \sim 0.5$, and the possibly associated molecular mass is shown to be $M < \sim 10^2$ and $< \sim 10^3 M_\odot$ for the near and far distances, respectively. Similar estimation applies to most of the observed partial CO shells in the analyzed SNR, but we do not present the results for individual objects, because the estimations are simply upper limits to the physically meaningful masses, which are supposed to be a few orders of magnitudes smaller, as discussed above.

4. SUMMARY

We obtained a systematic search by morphology for cavity and/or shell structures of ¹²CO and ¹³CO line emissions adjacent to 63 catalogued Galactic SNRs. Such a search was possible only by careful inspection of individual channel maps of brightness temperature with high-velocity and high-angular resolutions from the FUGIN CO survey. The result is presented in the form of a table of kinematical distances of the CO shells, and an atlas of CO-line T_B maps as superposed on the radio continuum maps of the SNRs, which will be useful for general purpose for the investigation of the interaction between SNRs and ISM in the Galaxy.

ACKNOWLEDGMENTS

We are grateful to Prof. Masumichi Seta of Kwansei Gakuin University and Dr. Hidetoshi Sano of the National Astronomical Observatory of Japan for helpful advises, and to Mr. Yuya Tsuda of Meisei University for discussion. The CO data were taken from the FUGIN CO survey obtained with the Nobeyama 45-m telescope, and retrieved from the JVO portal (<http://jvo.nao.ac.jp/portal>). The data analysis was carried out at the Astronomy Data Center of the National Astronomical Observatory of Japan. Radio continuum data were taken from the VGPS survey via the ATLASGAL data archives. The National Radio Astronomy Observatory is a facility of the National Science Foundation operated under cooperative agreement by Associated Universities, Inc.. This research is supported as part of the International Galactic Plane Survey through a Collaborative Research Opportunities grant from the Natural Sciences and Engineering Research Council of Canada.

Facilities: Nobeyama 45-m, VLA, Effelsberg 100-m

Software: astropy (Astropy Collaboration et al. 2013)

REFERENCES

- Astropy Collaboration, Robitaille, T. P., Tollerud, E. J., et al. 2013, A&A, 558, A33
- Chevalier, R. A. 1977, ARA&A, 15, 175
- Chevalier, R. A. 1999, ApJ, 511, 798
- Cox, D. P., Shelton, R. L., Maciejewski, W., et al. 1999, ApJ, 524, 179
- Deharveng, L., Schuller, F., Anderson, L. D., et al. 2010, A&A, 523, A6
- Fujita, S., Torii, K., Tachihara, K., et al. 2019, ApJ, 872, 49
- Fujita, Y., Ohira, Y., Tanaka, S. J., et al. 2009, ApJL, 707, L179
- Green, D. A. 2009, Bulletin of the Astronomical Society of India, 37, 45
- Green, D. A., & Dewdney, P. E. 1992, MNRAS, 254, 686
- Green, D. A. 2019, Journal of Astrophysics and Astronomy, 40, 36
- Helfand, D. J., Becker, R. H., White, R. L., et al. 2006, AJ, 131, 2525
- Honma, M., Nagayama, T., & Sakai, N. 2015, PASJ, 67, 70
- Jiang, B., Chen, Y., Wang, J., et al. 2010, ApJ, 712, 1147. doi:10.1088/0004-637X/712/2/1147
- Kilpatrick, C. D., Bieging, J. H., & Rieke, G. H. 2016, ApJ, 816, 1
- Koo, B.-C. & Moon, D.-S. 1997, ApJ, 475, 194. doi:10.1086/303527
- Koo, B.-C., & Moon, D.-S. 1997, ApJ, 485, 263
- Kuriki, M., Sano, H., Kuno, N., et al. 2018, ApJ, 864, 161
- Lee, Y.-H., Koo, B.-C., & Lee, J.-J. 2020, arXiv:2011.07711
- Lucas, W. E., Bonnell, I. A., & Dale, J. E. 2020, MNRAS, 493, 4700
- Maxted, N. I., Filipović, M. D., Hurley-Walker, N., et al. 2019, ApJ, 885, 129
- McKee, C. F., & Ostriker, J. P. 1977, ApJ, 218, 148
- Minamidani, T., Nishimura, A., Miyamoto, Y., et al. 2016, Proc. SPIE, 99141Z
- Paron, S., Ortega, M. E., Petriella, A., et al. 2012, A&A, 547, A60. doi:10.1051/0004-6361/201219953
- Paron, S. & Giacani, E. 2010, A&A, 509, L4. doi:10.1051/0004-6361/200913694
- Paron, S., Weidmann, W., Ortega, M. E., et al. 2013, MNRAS, 433, 1619. doi:10.1093/mnras/stt837
- Petriella, A., Paron, S. A., & Giacani, E. B. 2013, A&A, 554, A73. doi:10.1051/0004-6361/201321066
- Ranasinghe, S. & Leahy, D. A. 2017, ApJ, 843, 119. doi:10.3847/1538-4357/aa7894
- Ranasinghe, S. & Leahy, D. A. 2018, MNRAS, 477, 2243
- Reich, P., Reich, W., & Furst, E. 1997, A&AS, 126, 413
- Sano, H., Rowell, G., Reynoso, E. M., et al. 2019, ApJ, 876, 37. doi:10.3847/1538-4357/ab108f
- Sashida, T., Oka, T., Tanaka, K., et al. 2013, ApJ, 774, 10. doi:10.1088/0004-637X/774/1/10
- Seta, M., Hasegawa, T., Sakamoto, S., et al. 2004, AJ, 127, 1098
- Shull, J. M. 1980, ApJ, 237, 769
- Sofue, Y. 2020, Galaxies, 8, 37
- Sofue, Y. & Kohno, M. 2020, MNRAS, 497, 1851
- Stil J. M., et al., 2006, AJ, 132, 1158
- Su, Y., Chen, Y., Yang, J., et al. 2009, ApJ, 694, 376. doi:10.1088/0004-637X/694/1/376
- Su, Y., Chen, Y., Yang, J., et al. 2011, ApJ, 727, 43. doi:10.1088/0004-637X/727/1/43
- Su, Y., Zhang, S., Shao, X., et al. 2015, ApJ, 811, 134. doi:10.1088/0004-637X/811/2/134
- Su, Y., Zhou, X., Yang, J., et al. 2017, ApJ, 836, 211. doi:10.3847/1538-4357/aa5cb7
- Tatematsu, K., Fukui, Y., Landecker, T. L., et al. 1990, A&A, 237, 189
- Tian, W. W., Leahy, D. A., & Wang, Q. D. 2007, A&A, 474, 541
- Umemoto, T., Minamidani, T., Kuno, N., et al. 2017, PASJ, 69, 78
- Voisin, F., Rowell, G., Burton, M. G., et al. 2016, MNRAS, 458, 2813. doi:10.1093/mnras/stw473
- Yang, J., Zhang, J.-L., Cai, Z.-Y., et al. 2006, ChJA&A, 6, 210. doi:10.1088/1009-9271/6/2/8
- Yoshiike, S., Fukuda, T., Sano, H., et al. 2013, ApJ, 768, 179. doi:10.1088/0004-637X/768/2/179
- Zhou, X., Chen, Y., Su, Y., et al. 2009, ApJ, 691, 516. doi:10.1088/0004-637X/691/1/516
- Zhu, H., Tian, W. W., & Zuo, P. 2014, ApJ, 793, 95. doi:10.1088/0004-637X/793/2/95
- Ziurys, L. M., Snell, R. L., & Dickman, R. L. 1989, ApJ, 341, 857. doi:10.1086/167544

APPENDIX

A. SNR DISTRIBUTION

Figure 4 shows the positions of the SNRs from the Green's catalogue on the CO line brightness map (red: ^{13}CO , green: ^{12}CO , blue: C^{18}O).

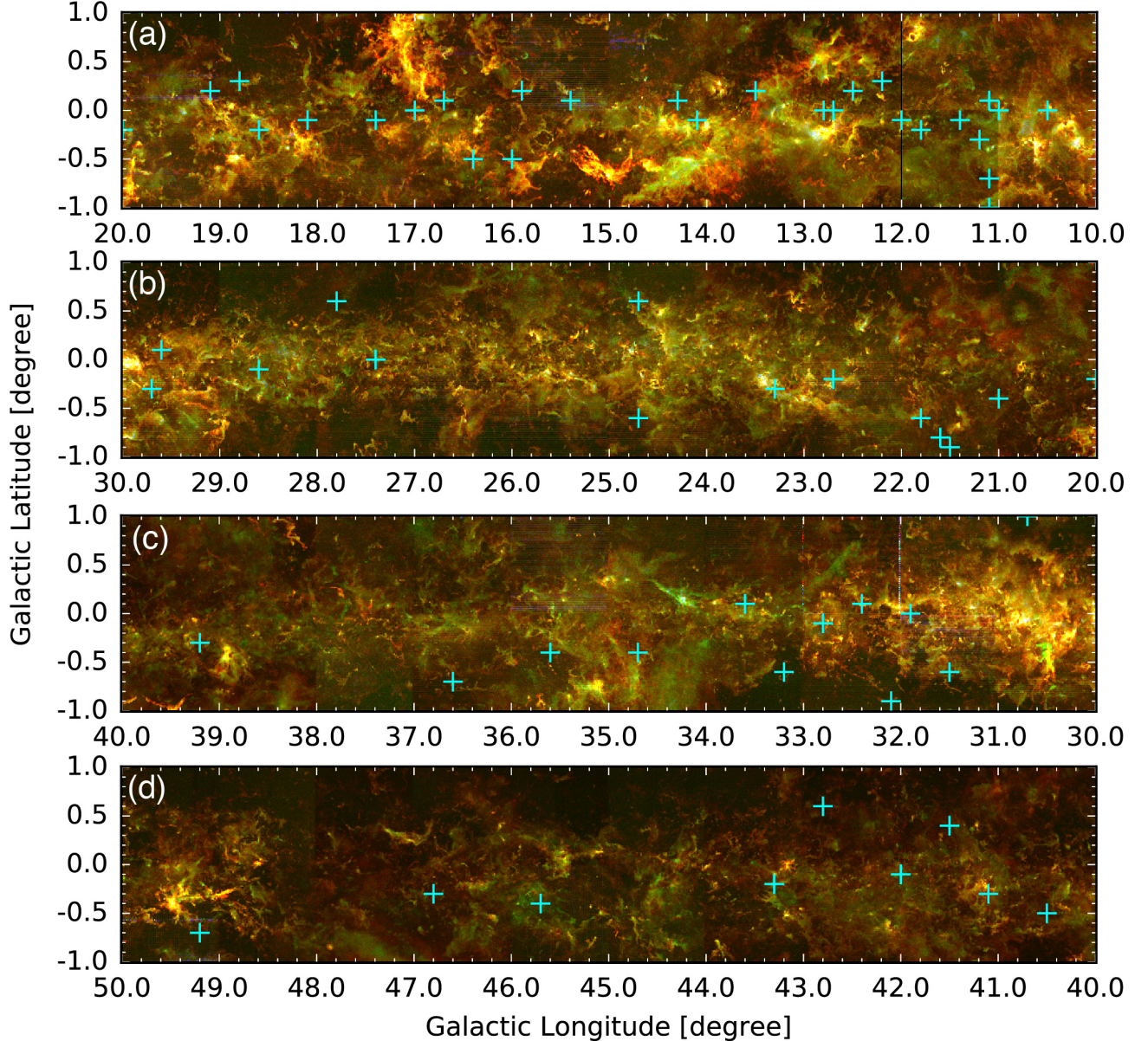


Figure 4. Green's SNRs (cyan crosses) superposed on the FUGIN CO map (<https://nro-fugin.github.io>) of the peak brightness temperatures of ^{12}CO , ^{13}CO and C^{18}O lines in red, green and blue, respectively (Umemoto et al. 2017). The Galactic longitude range of (a) $10^\circ \leq l \leq 20^\circ$, (b) $20^\circ \leq l \leq 30^\circ$, (c) $30^\circ \leq l \leq 40^\circ$, and (d) $40^\circ \leq l \leq 50^\circ$, respectively.

B. TABLE OF SNRS

Table B lists the analyzed objects and derived parameters for the candidate CO line features adjacent to the SNRs.

Table 2. CO-line cavities and shells toward SNRs from the Green's catalogue.

(a) l, b ($^{\circ}$, $^{\circ}$)	(b) v_{lsr} (km/s)	(c) Size ($' \times '$)	(d) SNR	(e) $f_{1\text{GHz}}$	(f) Type [†]	(g) κ in %	(h) d_{near} (kpc)	(i) d_{far} (kpc)	(j) δd (kpc)	(k) D_{near} (pc)	(l) D_{far} (pc)	(m) Name	References
11.00-0.05	+40	11 9	S	1.3	Sh 50	6	11.6	0.3	12.0	33.4			
11.1-0.7	+33	11 7		1.0	Ps 50	3.5	12.2	0.3	8.9	31.2			
(11.1 +0.1)	—	12 10	S	2.3	N								
11.17-0.35	+33	4 4	C	22	Ca 50	3.7	12.0	0.3	4.3	14.0		15	
11.2+0.12	+56	12 10	S	2.3	Ps 30	6	10.8	0.2	11.6	25.7			
11.4-0.1	+30	8 8	S?	6	Ca 60	3.4	12.3	0.3	8.0	28.5			
—	+50				Ca 50	4.1	11.5	0.3	9.6	26.9			
11.89-0.23	+49.8	4 4	F	0.7	Ca 50	4.5	11.1	0.2	5.3	13.0			
12.0 -0.1	+37.4	7 7 ?	?	3.5	Ps 50	3.8	11.8	0.3	7.7	24.1			
(12.2 +0.3)	—	6 5	S	0.8	N								
(12.5 +0.2)	—	6 5	C?	0.6	N								
(12.7 -0.0)	—	6	S	0.8	N								
(12.8 -0.0)	—	3	C?	0.8	N								
13.45+0.14	+24	5 4	S	3.5?	Ca 50	2.7	12.9	0.2	3.5	16.8			
(14.1 -0.1)	—	6 5	S	0.5	N								
(14.3 +0.1)	—	5 4	S	0.6	N								
15.42+0.16	+34	15 14	S	5.6	Sh 60	3.2	12.3	0.3	13.3	51.7			
15.9+0.2	+29	7 5	S?	5.0	Ps 50	2.8	12.6	0.3	4.8	21.7			
(16.0 -0.5)	—	15 10	S	2.7	N								
(16.4 -0.5)	—	13 13	S	4.6	N								
16.75+0.08	+47	4 4	C	3.0	Ca 90	3.8	11.6	0.3	4.4	13.5			
—	+62				Ps 50	4.5	10.9	0.2	5.2	12.6			
17.05-0.05	+31.0	6 6	S	0.4	Ca 50	2.8	12.5	0.3	4.1	18.2			
—	+93.4	6 6	S	1.4	Ca 30	5.6	9.7	0.2	8.2	14.1			
18.1-0.1	+49	8 8	S	4.6	Ps 50	3.7	11.5	0.3	8.7	26.7		10, 21	
18.6 -0.2	+66	6 6	S	1.4	Ca 50	4.5	10.7	0.2	7.8	18.7		16	
18.8+0.35	+20	17 11	S	33	Ps 60	1.9	13.3	0.4	7.4	52.8	Kes 67	9	
(19.1 +0.2)	—	27 27	S	10	N								
20.0-0.2	+65	10 10	F	10	Ca 60	4.3	10.7	0.2	12.6	31.2		11	
(20.4 +0.1)	—	8 8	S?	9?	N								
(21.0 -0.4)	—	9 7	S	1.1	N								
(21.5 -0.9)	—	5 5	C	7	No 20cm								
(21.6-0.8)	—	13	S	1.4	No 20cm								
21.8-0.6	+83	20 20	S	65	Sh 70	5.0	9.9	0.2	28.9	57.6	Kes 69	4, 21	
22.7-0.2	+75	26 26	S?	33	Ps 60	4.6	10.2	0.2	34.7	76.9		14	
23.3-0.3	+70	27 27	S	70	Ps 70	4.3	10.4	0.2	34.1	81.3	W41	14	
(23.6 +0.3)	—	10 10	?	8?	N								
24.7-0.6	+60	15 15	? S?	8	Ca 30	3.8	10.7	0.3	16.7	46.7		19	
24.7+0.6	+112	30 15	C?	20?	C/P 60	6.3	8.2	0.4	39.1	50.6			

[†] "N" stands for no possible cavity/shell in CO recognized. Columns (a),(c),(d),and (e) are from Green's catalogue(Green 2009).

Columns: (a) Galactic position; (b) CO line radial velocity from the present measurements using FUGIN; (c) apparent major and minor-axis sizes, θ_x, θ_y ; (d) SNR type; (e) radio flux at 1 GHz; (f) CO cavity or shell measure; (g) near solution of the distance for the CO radial velocity; (h) far distance; (i) distance error; (j)linear diameter for near distance $D = \sqrt{\theta_x \theta_y} d$; (k) for far distance, (l) Name, (m) References to other CO-line observations: 1) Koo & Moon (1997); 2) Seta et al. (2004); 3) Yang et al. (2006); 4) Zhou et al. (2009); 5) Su et al. (2009); 6) Jiang et al. (2010); 7) Paron & Giacani (2010); 8) Su et al. (2011); 9) Paron et al. (2012); 10) Paron et al. (2013); 11) Petriella et al. (2013); 12) Yoshiike et al. (2013); 13) Zhu et al. (2014); 14) Su et al. (2015); 15) Kilpatrick et al. (2016); 16) Voisin et al. (2016); 17) Su et al. (2017); 18) Ranasinghe & Leahy (2017); 19) Ranasinghe & Leahy (2018); 20) Kuriki et al. (2018); 21) Lee et al. (2020).

Table 2. Continued.

l, b ($^{\circ}, {}^{\circ}$)	v_{lsr} (km/s)	Size ($' \times '$)	SNR type	$f_{1\text{GHz}}$ (Jy)	Type (κ in %)	d_{near} (kpc)	d_{far} (kpc)	δd (kpc)	D_{near} (pc)	D_{far} (pc)	Name	References
27.4+0.0	+101	4 4	S	6	Ca 60	5.8	8.4	0.4	6.8	9.8	4C-04.7	15
(27.8 +0.6)	—	50 30	F	30	N							
28.62-0.10	+86	13 9	S	3?	Ca 60	5.0	9.0	0.3	15.7	28.5		19
29.6 +0.1	+99.2	5	S	1.5?	Sh 50	5.9	8.0	0.5	8.6	11.7		15
29.70-0.26	+52	3 3	C	10	Ca 50	3.3	10.6	0.3	2.9	9.3	Kes 75	5
—	+112				Ps 40	3.3	10.6	0.3	2.9	9.3		
31.5-0.6	+87.5	18 18?	S?	2?	Ps 50	5.2	8.4	0.3	27	44		
—	+97				Ca 40	6.0	7.6	0.5	31	40		
31.9+0.0	+107	7 5	S	25	Ca 50	6.8	6.8	—	12	12	3C391	18
32.1-0.9	+95	40 40?	C?	?	N	5.9	7.7	0.5	69	89		
32.4+0.1	+10.8	6 6	S	0.25?	Ca 100	0.79	12.7	0.2	1.4	22		
—	+42.6				Ca 30	2.7	10.8	0.2	4.8	18.8		15
32.8 -0.1	+74	17 17	S?	11?	Ps 10	4.4	9.0	0.25	22	45	Kes 78	
—	+103				Ca 30	6.7	6.7	—	33	33	Kes 78	
33.2 -0.6	+54	18 18	S	3.5	Ps 20	3.3	10.1	0.2	17	53		
—	+91				Ca 10	5.7	7.7	0.5	30	40		
33.7+0.05	+70	10 10	S	20	Ca 70	4.2	9.1	0.3	12.3	26.4	Kes 79	20
34.7-0.4	+40	35 27	C	250	Ca 60	2.6	11	0.2	23	95	W44	2
—	+52				Ca 75	3.2	9.9	0.2	29	89	W44	12
35.6 -0.4	+55	15 11	S?	9	Ca 40	3.4	9.6	0.2	13	36		7
—	+90				Pa 20	6.5	6.5	—	24	24		
36.6-0.7	+57	25 25?	S?	1.0	Ca 20	3.5	9.3	0.3	26	68		
—	+79				Ca 20	5.1	7.8	0.4	37	57		
39.2-0.3	+51	8 6	C	18	Ca 30	3.2	9.2	0.3	6.5	18.5	3C396	21
—	+67				Ca 60	4.3	8.1	0.5	8.7	16.2		8
40.5 -0.5	+58	22 22	S	11	Ca 70	3.8	8.4	0.3	24	54		3
41.1 -0.3	+32	4.5 2.5	S	25	Ca 60	2.1	10.0	0.3	2.0	9.7	3C397	6
—	+38				Ca 100	2.5	9.6	0.3	2.4	9.4		
41.5+0.4	+58	10 10	S?	1?	Ca 50	3.8	8.2	0.4	11	24		
42.0-0.1	+66	8x8	S?	0.5?	Ca 60	4.6	7.3	0.5	11	17		
(42.8 +0.6)		24 24	S	3?	N							
43.3-0.2	+10	4 3	S	38	Ca 50	0.7	11	0.3	0.7	11	W49B	21
—	+45				Ca 60	3.0	8.7	0.3	3.0	8.7	W49B	13, 21
—	+62				Ca 100	4.4	7.3	0.7	4.4	7.3	W49B	21
45.7 -0.4	+26	22 22	S	4.2?	Pa 40	1.8	9.4	0.3	11	60		
—	+48.5				Pa 20	3.4	7.8	0.4	22	50		
46.8-0.3	+52	15	S	17	Ca 70	3.9	7.1	0.5	17	31	HC30	
49.2 -0.7	+50	30 30	S?	160?	Pa 30	4.1	6.4	0.7	35	56	W51C	1
—	+60	30 30	S?	160?	Ca 50	5.2	5.2	—	46	46	W51C	
205.5 +0.5	+10	220	S	140	N	0.98	—	0.3	63	—	Monoceros	17
—	+20				N	2.2	—	0.3	139	—	Monoceros	
213.0 -0.6	+9	160x140?	S	21	0.4 N	0.7	—	0.3	32	—		17
—	+21				N	1.8	—	0.3	80	—		

G11.00-0.05+40 km s⁻¹

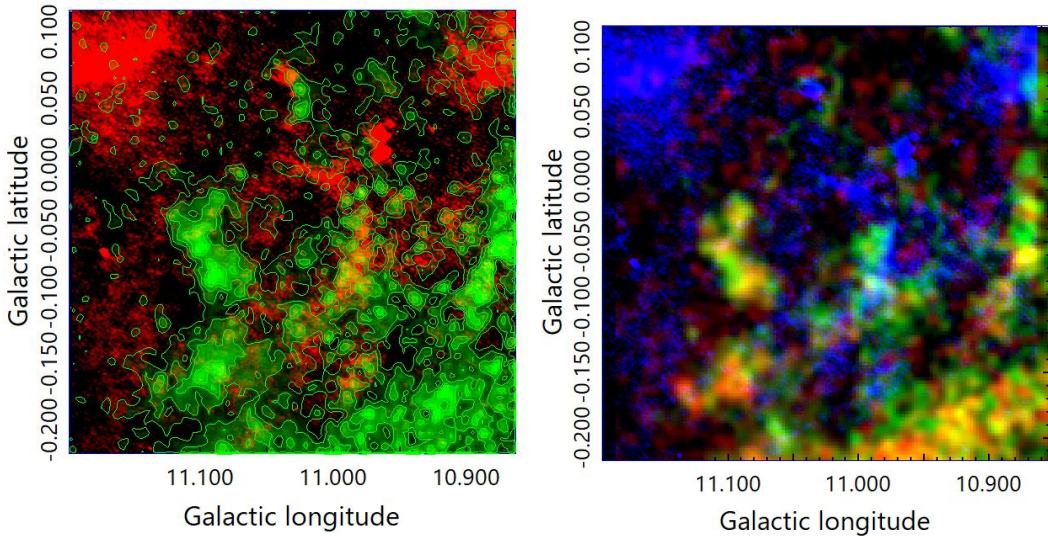


Figure 5. Same as figure 2, but for SNR G11.00-0.05+40.725, 40.075 km s⁻¹: (Left) ^{12}CO contours superposed on the radio continuum map in red. Contours start at 2K by step 1K. (Right) Two color composite image of CO T_{B} , red and green showing ^{12}CO and ^{13}CO respectively, superposed on 20-cm radio map.

G11.1-0.7, +33.6 km s⁻¹

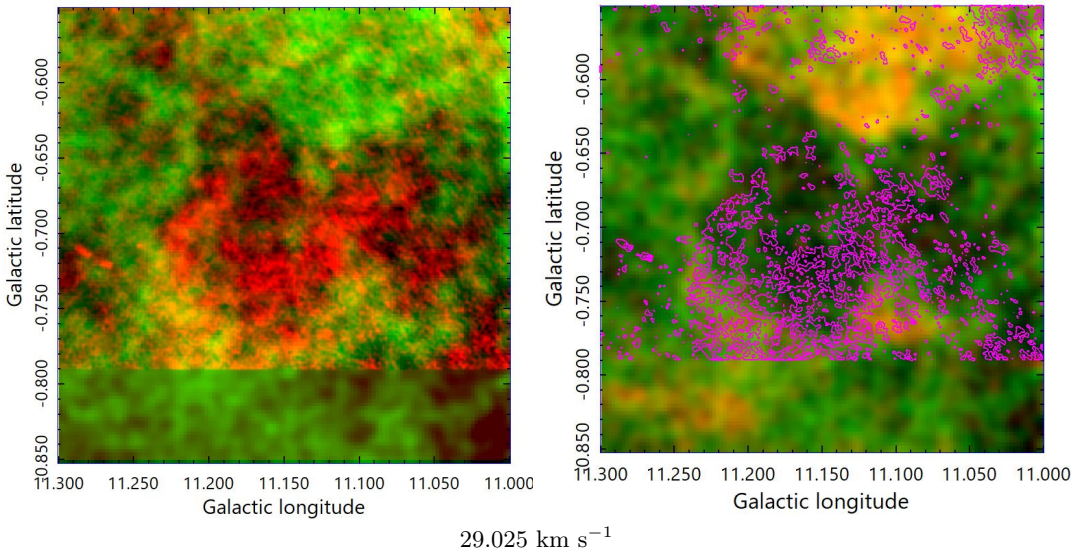


Figure 6. Same as figure 2, but for SNR G11.1-0.7, 33 km s⁻¹: (Left) $^{12}\text{CO} T_{\text{B}}$ in green (from 0 to 10 K) superposed on 20 cm brightness map in red. (Right) Composite CO map of co and $^{13}\text{CO} T_{\text{B}}$ (R(^{13}CO , 0 - 4K), G(^{12}CO , 0 - 12K)) on radio 20-cm contour map (from 0.5, step 0.5 mJy beam⁻¹).

C. FIGURES

Figures 5 to 51 show the analyzed results on individual SNRs.

G11.17-0.35+33 km s⁻¹

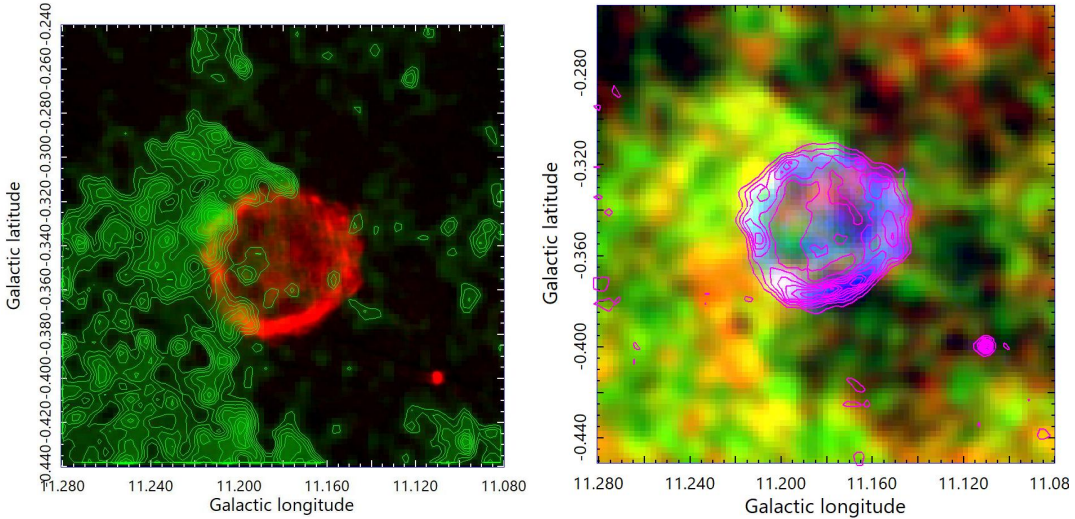


Figure 7. Same as figure 2, but for SNR G11.18-0.35+32.925km s⁻¹: (Left) ^{12}CO contour map (from 7K by 0.5K) superposed on 20cm radio in red color. (Right) Two-color map of ^{12}CO in green and ^{13}CO in red superposed on the 20-cm contour map (start 5, step 5 mJy beam⁻¹).

G11.2+0.12+55 km s⁻¹

55.025 56.975 km s⁻¹

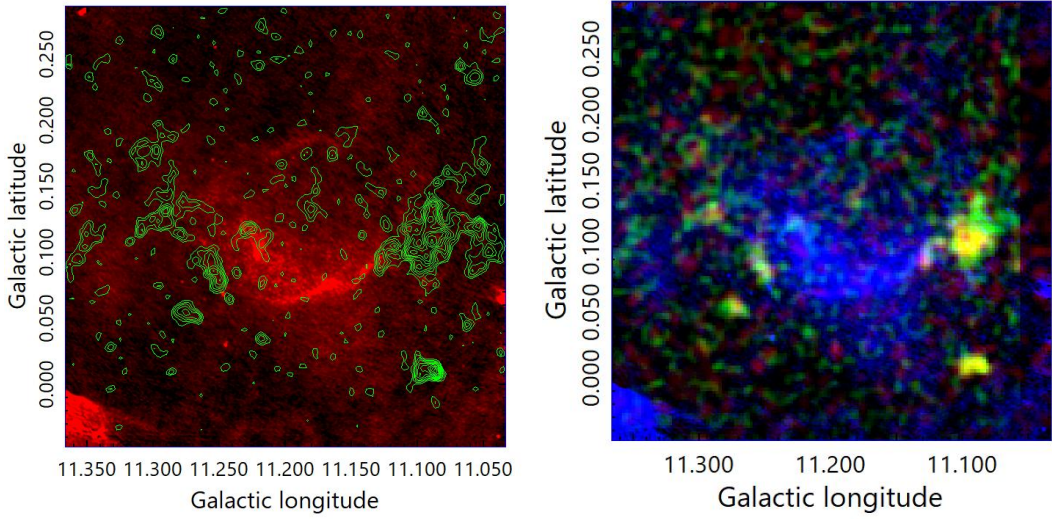


Figure 8. Same as figure 2, but for SNR G11.2+0.12+55 km s⁻¹. (Left) ^{12}CO T_B contour map (start 2K, step 2K) superposed on 20-cm radio continuum map in red (0 to 3 mJy beam⁻¹). (Right) Two-color CO T_B map (^{12}CO in green (0 to 8 K), ^{13}CO in red (0 to 2.5 K)) superposed on 20-cm map in blue (from 0.5 to 2 mJy beam⁻¹).

G11.4-0.1, +30 km s⁻¹

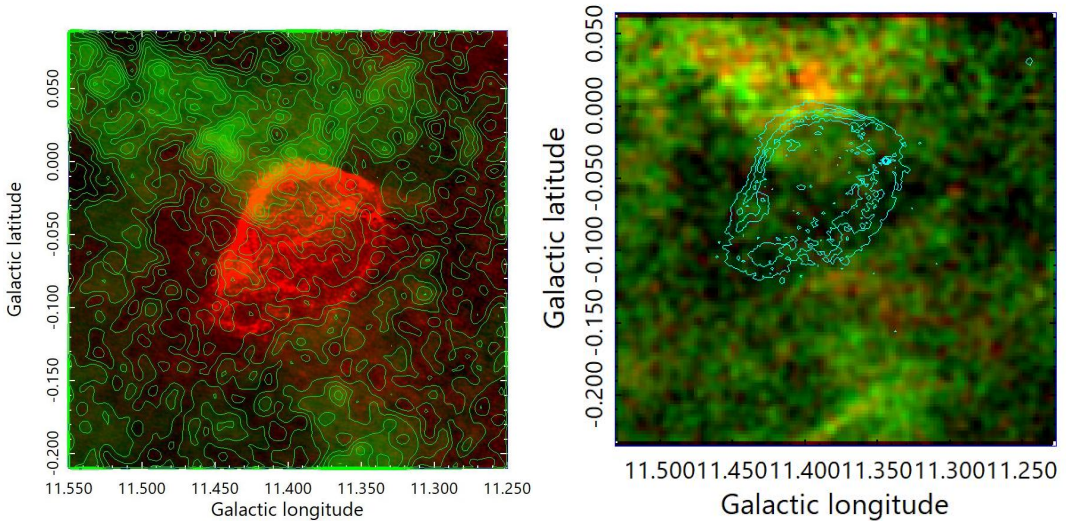
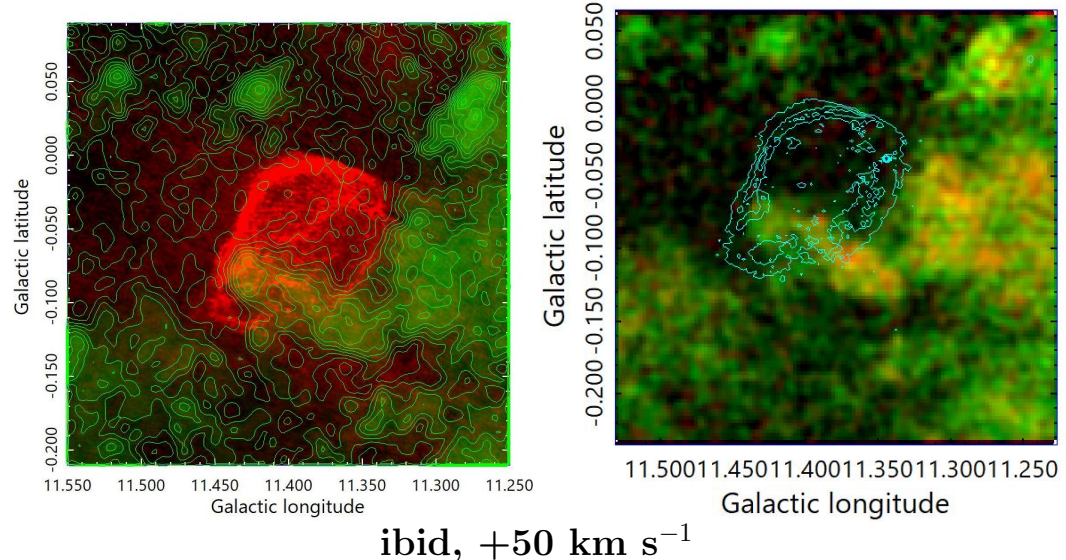


Figure 9. Same as figure 2, but for SNR G11.4-0.1+30.325, +49.875 km s⁻¹: (Left) ¹²CO contours (start at 1K, step 1K) superposed on 20 cm radio map in red. (Right) ¹³CO in red color (0 to 5K) and ¹²CO in green (0 to 10K), superposed on 20 cm contour map from (0.5 to 2 mJy beam⁻¹).

G11.89-0.23, +49.825 km s⁻¹

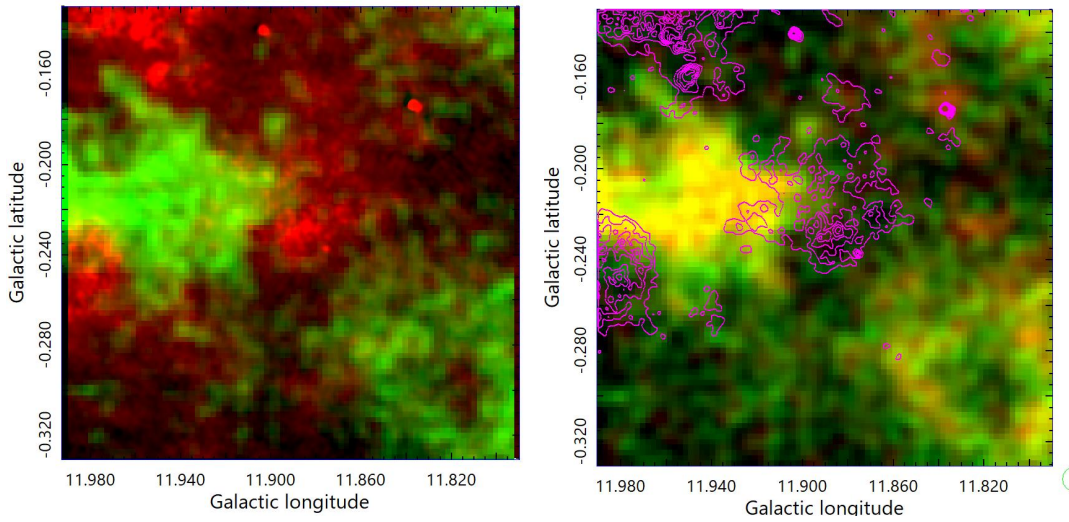


Figure 10. Same as figure 2, but for SNR G11.89-0.23, +49.825 km s⁻¹, ¹³CO R(0-3K), ¹²CO G(0-10K), cont.(start 1.5 step 0.5 mJy beam⁻¹).

G12.0-0.1+37 km s⁻¹

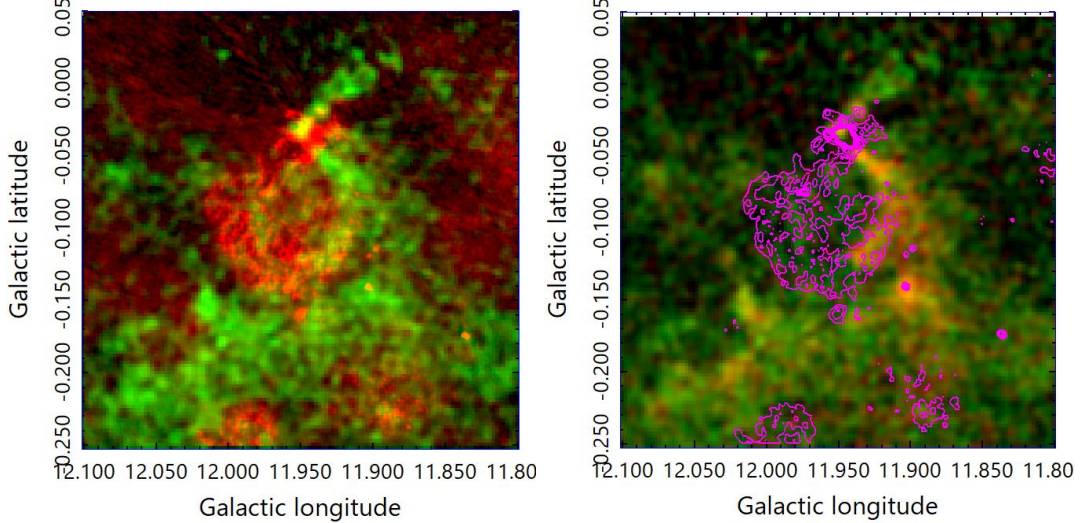


Figure 11. Same as figure 2, but for SNR G12.0-0.1+37, +37.475 km s⁻¹, ¹³CO R(0-6K), ¹²CO G(0-15K), 20cm cont. start 2 step 2 mJy beam⁻¹).

G13.45+0.14+24 km s⁻¹

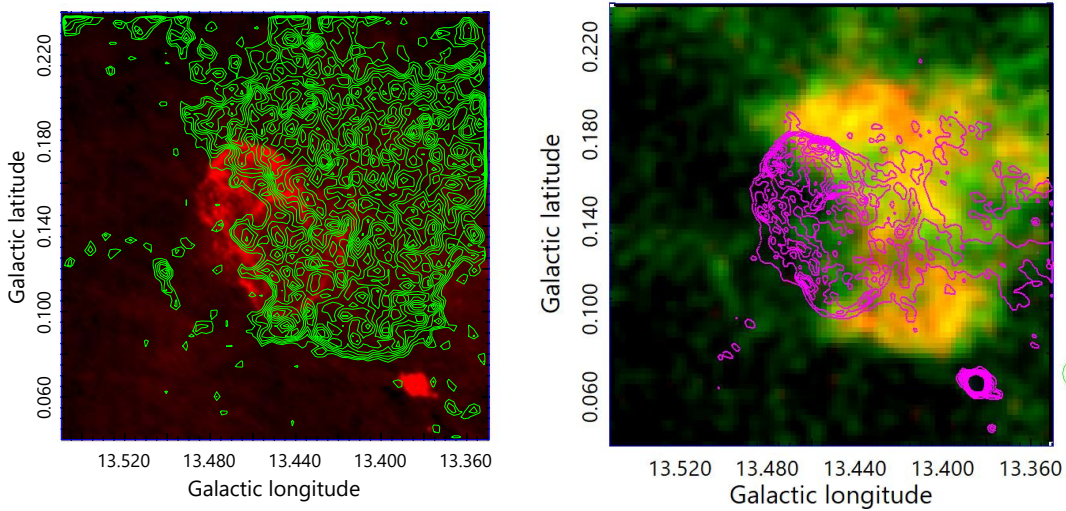


Figure 12. Same as figure 2, but for SNR G13.45+0.14+24 km s⁻¹; ¹²CO start 5K step1 K; 20cm start 0 step 7 mJy beam⁻¹. R(1-5K)/G(1-15K)/Cont(2by1mJy), 24.475 km s⁻¹

G15.42+0.16+34 km s⁻¹

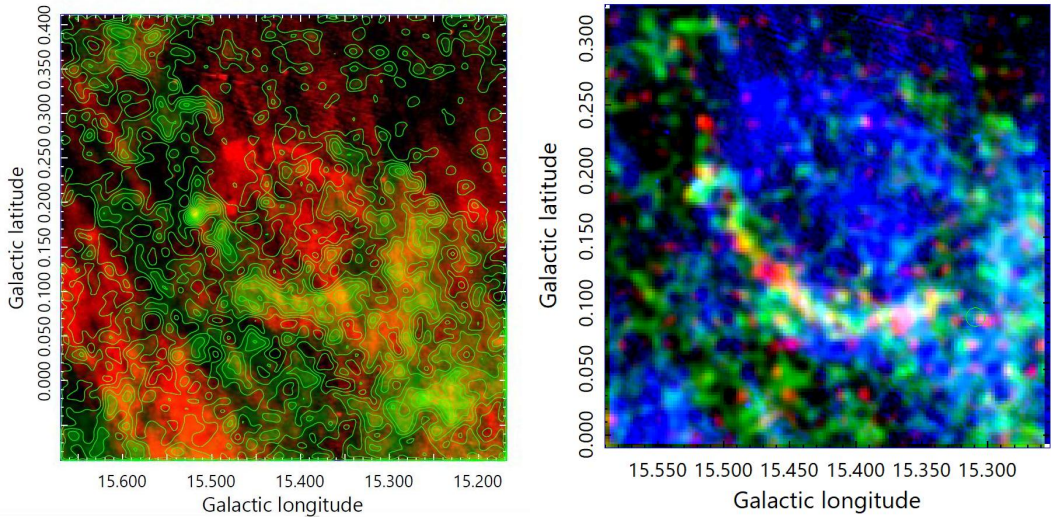


Figure 13. Same as figure 2, but for SNR G15.42+0.16, 34.225 km s⁻¹; ¹²CO contours start at 1K with step 1K.

G15.9+0.2+29 km s⁻¹

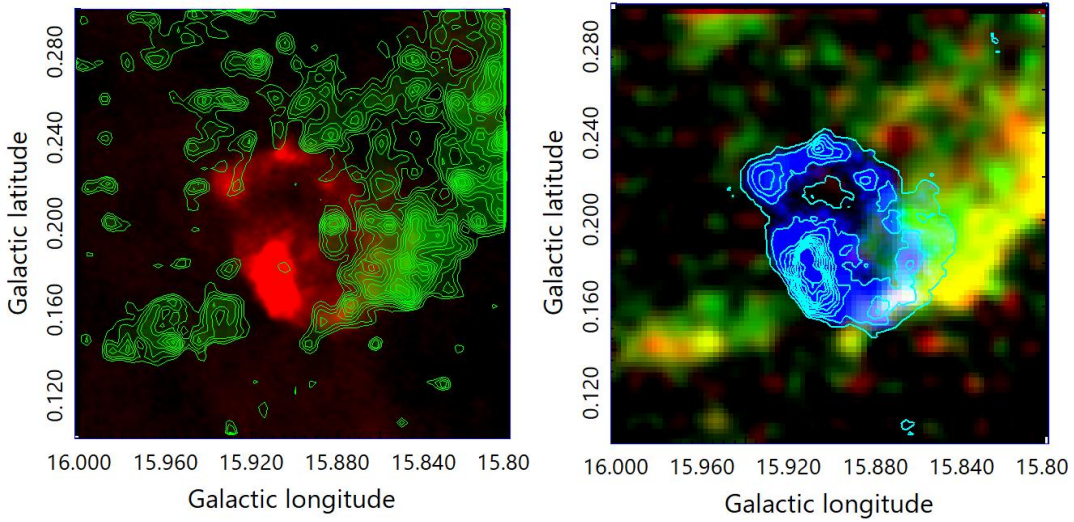


Figure 14. Same as figure 2, but for SNR G15.9+0.2+29. (Left) ^{12}CO contours start at 5 K by step 1 K superposed on 20 cm in red ($0 - 5 \text{ mJy beam}^{-1}$). (Right) $R(^{13}\text{CO} 0.5\text{-}4\text{K}) / G(^{12}\text{CO} 2\text{-}12\text{K}) / B(20 \text{ cm contours } 0\text{-}8\text{mJy beam}^{-1})$.

G16.75+0.08, +47 km s⁻¹

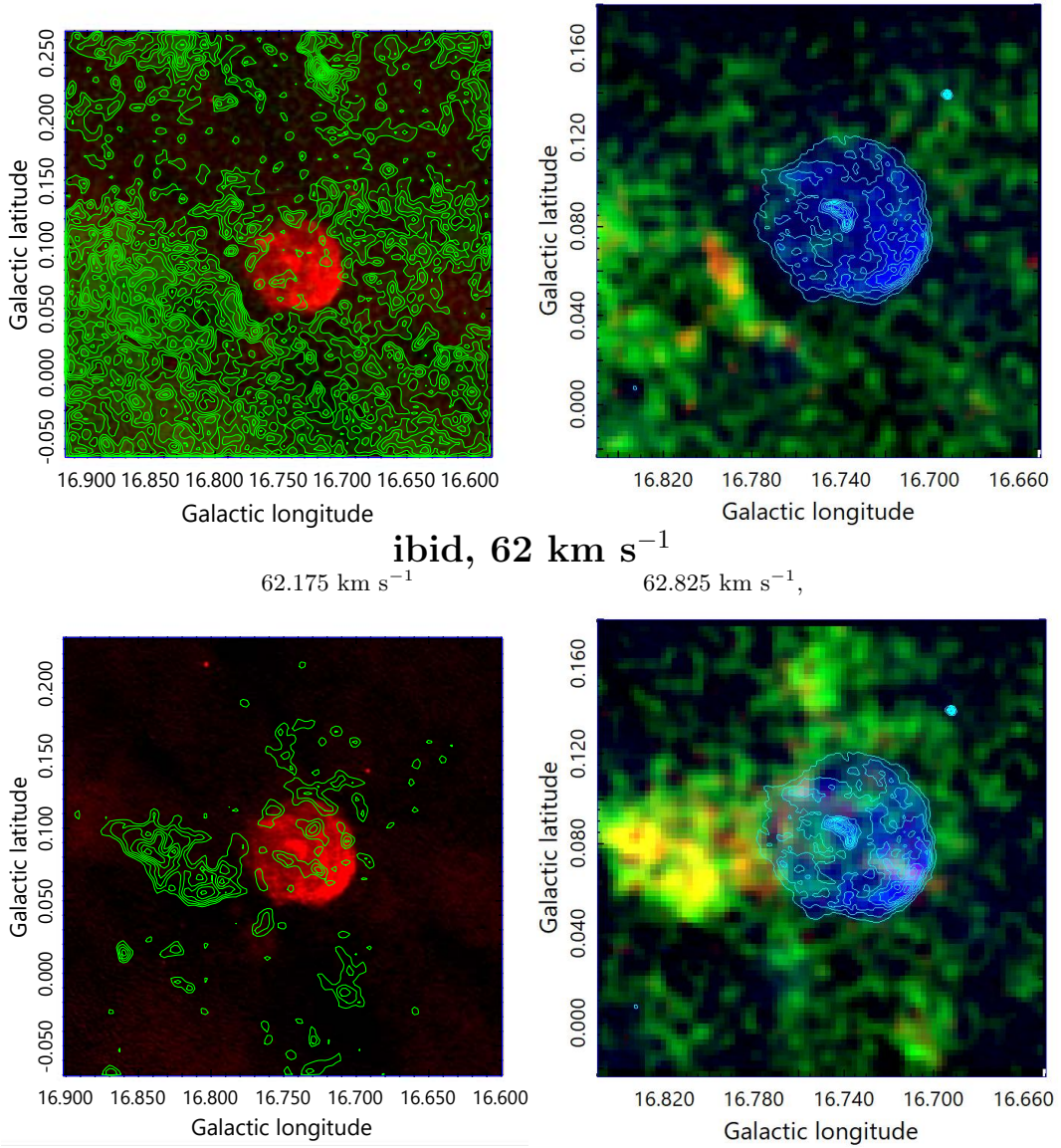


Figure 15. Same as figure 2, but for SNR G16.75+0.08, 47 km s⁻¹(¹²CO from 2K by 1K; 20 cm from 0 by 4 mJy), or 62 km s⁻¹(4K, 1K; 0, 8mJy).

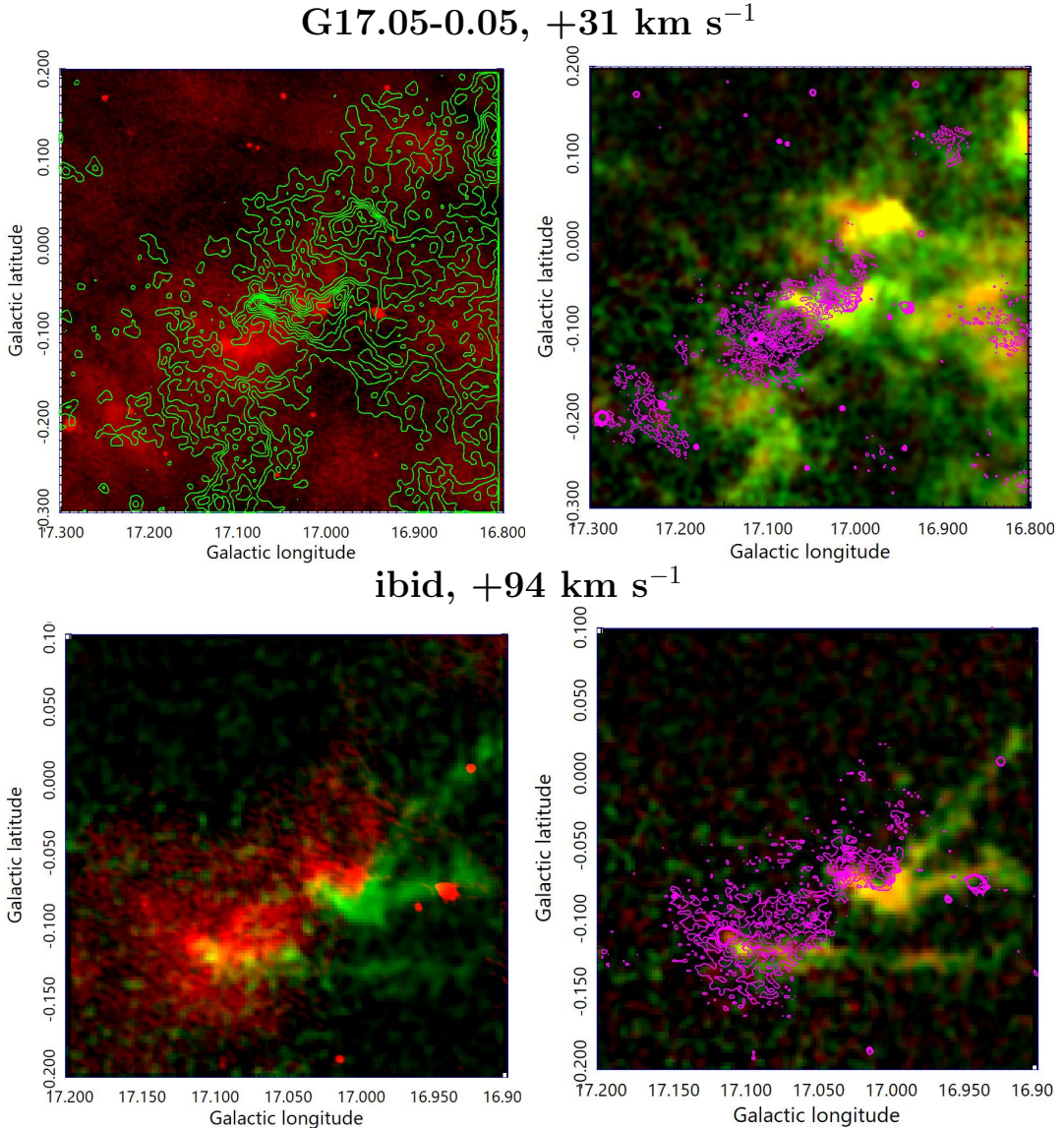


Figure 16. Same as figure 2, but for SNR G17.05-0.05, 94 km s⁻¹. (Top) 30.975 km s⁻¹, G(¹²CO) on R(20 cm) auto; R(¹³CO 0-5K) G(¹²CO 0-15K) on 20-cm cont. (from 1 by 0.25mJy beam⁻¹). (Bottom) 94.025, G(¹²CO) on R(20 cm) auto; 93.375 R(¹³CO 0-5K), G(¹²CO 0-15K), cont.(20 cm 1 by 0.25mJy beam⁻¹)

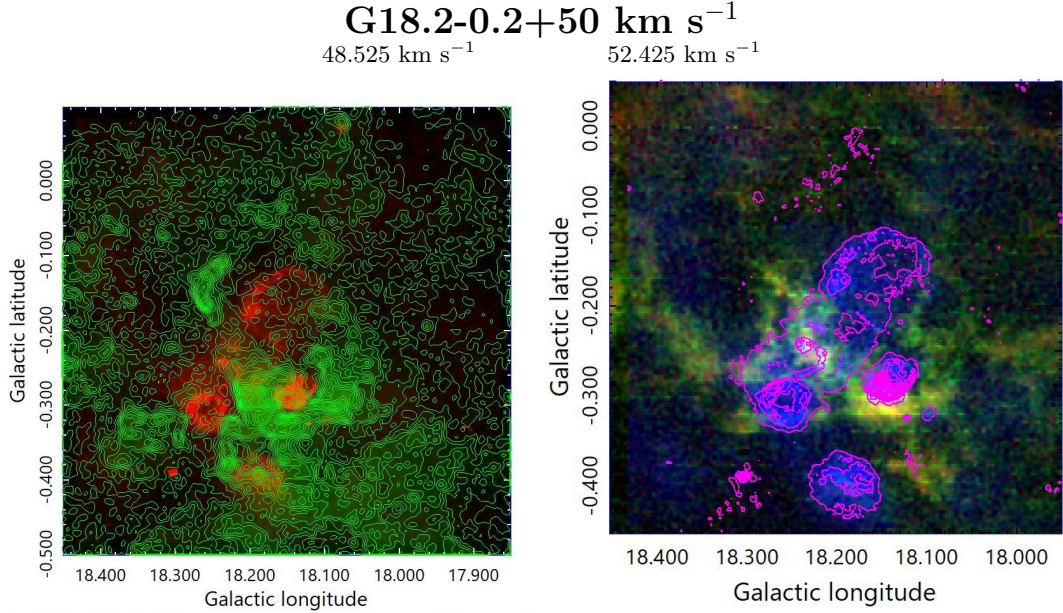


Figure 17. Same as figure 2, but for SNR G18.2-0.2, 48.525 km s^{-1} . ^{12}CO contours on 20 cm in red ($0\text{-}2\text{mJy beam}^{-1}$). $R(^{13}\text{CO } 0 \text{ to } 15 \text{ K}) / G(^{12}\text{CO } 0 \text{ to } 40 \text{ K})$ /contours (20 cm; start 2, step 1 mJy beam $^{-1}$)

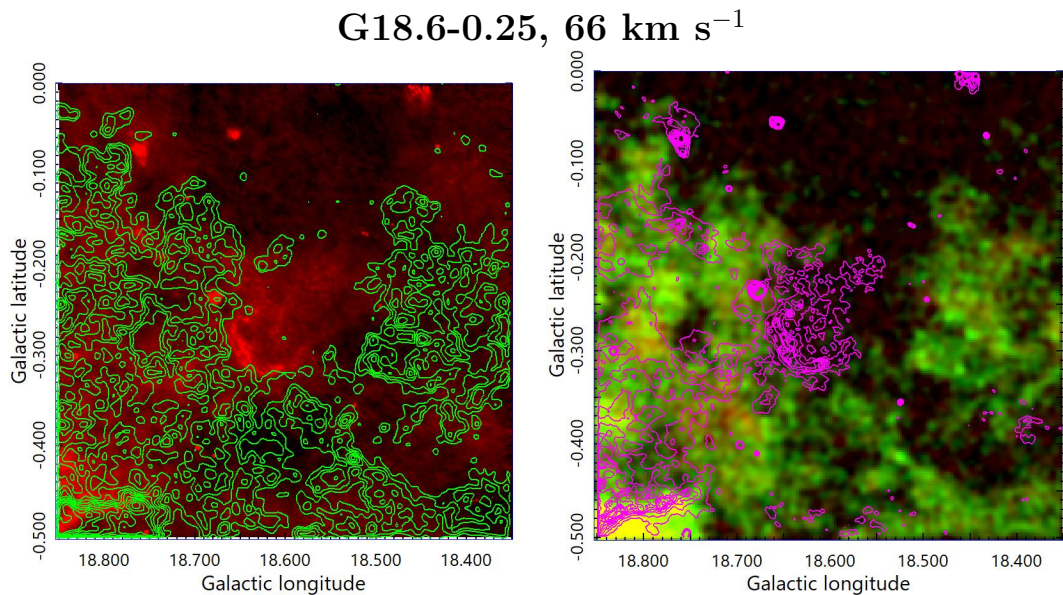


Figure 18. Same as figure 2, but for G18.6-0.25+66 km s $^{-1}$. ^{12}CO contours at 66.075 km s^{-1} on 20cm auto; $R(^{13}\text{CO } 0 \text{ - } 5 \text{ K}) / G(^{12}\text{CO } 0 \text{ - } 15 \text{ K})$ / contours (20 cm; start 1.5, step 4 mJy beam $^{-1}$)

G18.8+0.35 +20, Kes 67

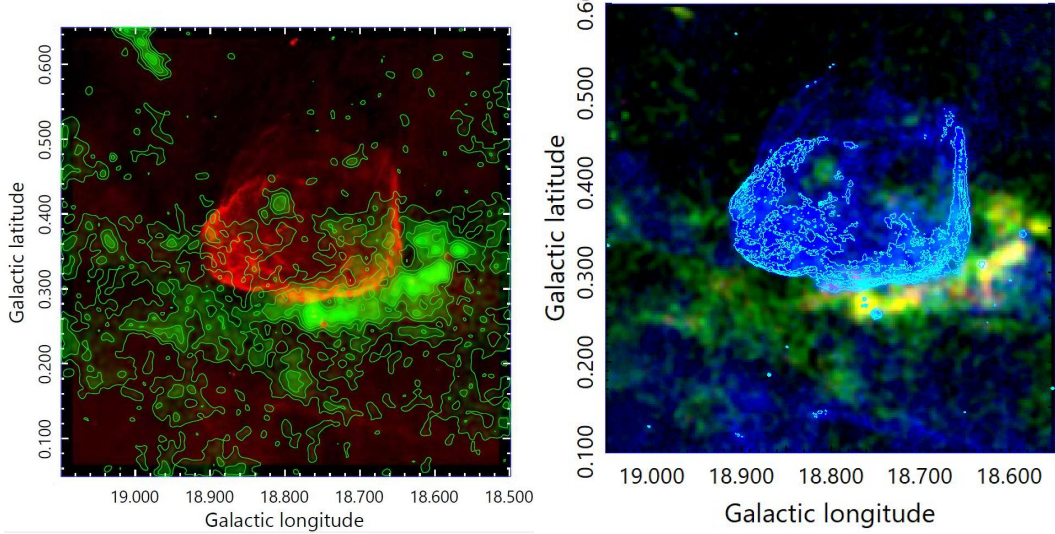


Figure 19. Same as figure 2, but for G18.8+0.35, $+20 \text{ km s}^{-1}$ superposed on 20 cm in red (auto). R (^{13}CO 1 - 5 K) / G(^{12}CO 1 - 12 K)/contours (20cm, start 2, step 2 mJy beam $^{-1}$).

G20.0-0.2+65 km s $^{-1}$

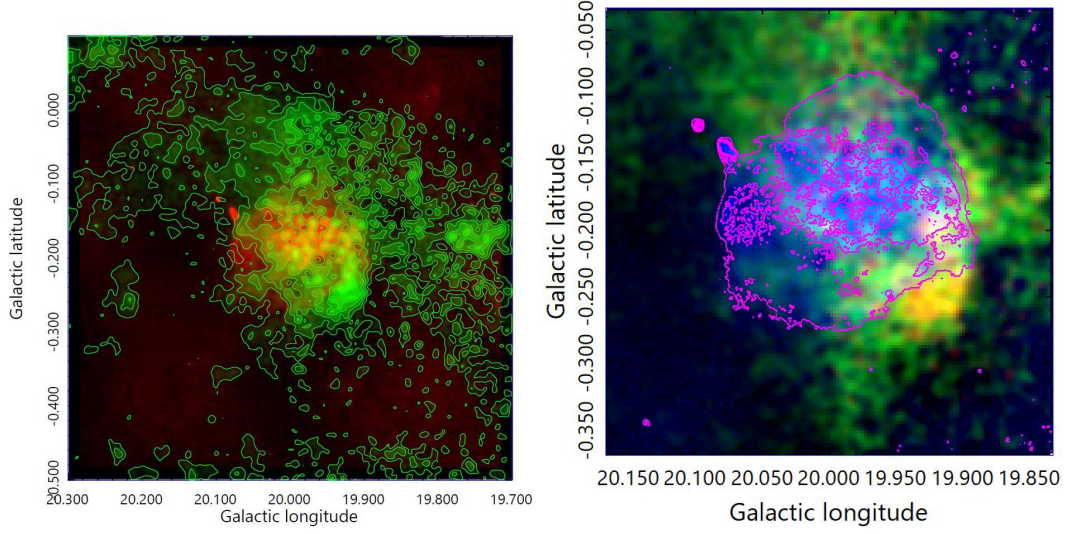


Figure 20. Same as figure 2, but for G20.0-0.2, 64.775 km s^{-1} : ^{12}CO on 20 cm (auto); R (^{13}CO 1 - 6 K) / G(^{12}CO 1 - 12 K) / contours (20 cm, start 1, step 1 mJy beam $^{-1}$).

G21.8-0.5+83 km s⁻¹, Kes 69

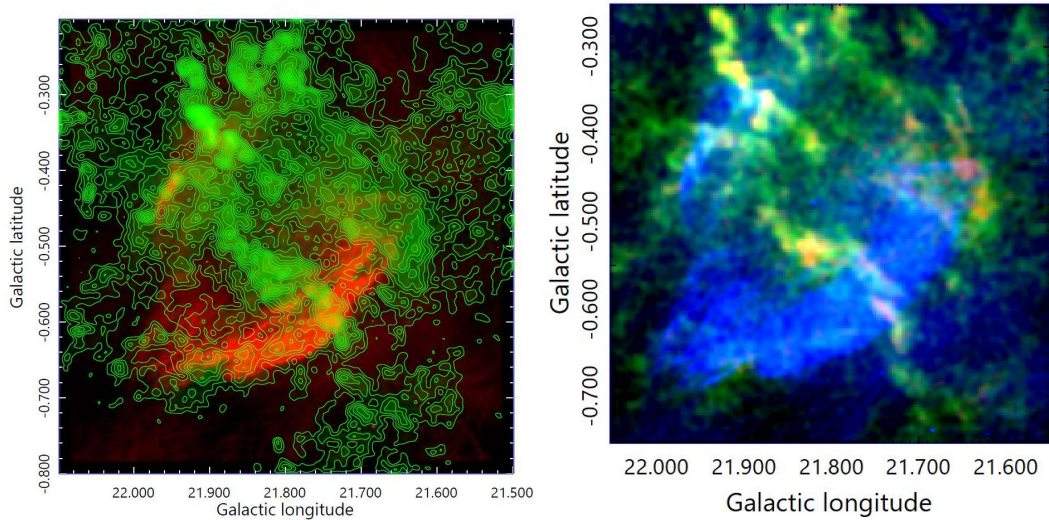


Figure 21. Same as figure 2, but for G21.18-05+82.975 km s⁻¹^{¹²}CO contour start 4K, step 1K superposed on 20 cm in red. R(^{¹³}CO , 1 to 4 K) / G(^{¹²}CO , 1 to 12 K) / 20 cm (0 to 3 mJy beam⁻¹).

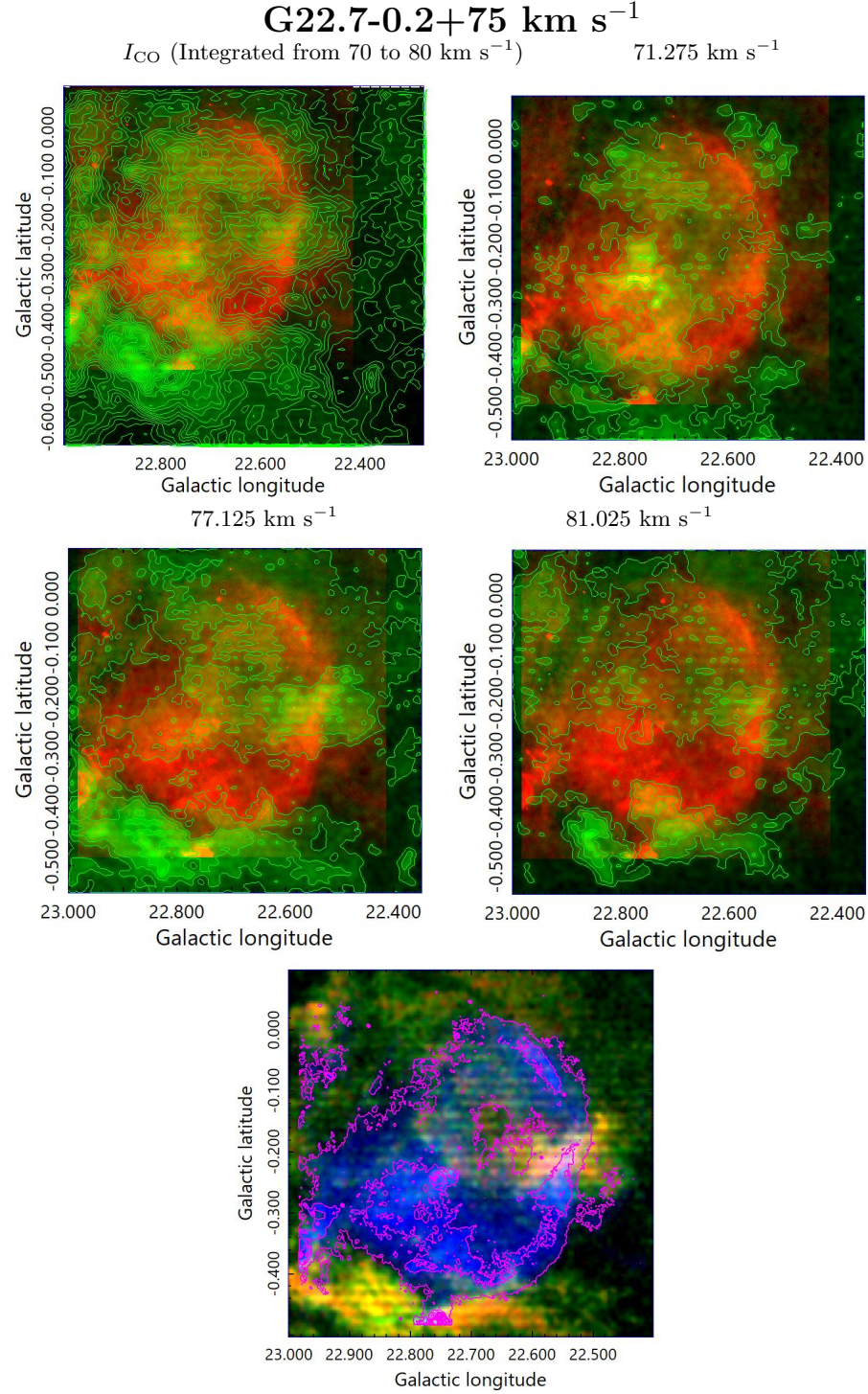


Figure 22. Same as figure 2, but for G22.27-0.2+75 km s⁻¹. (Top left) I_{CO} integrated from 70 to 80 km s⁻¹, contours start at 25, step 25 K km s⁻¹; (Top right and middle) ^{12}CO T_B at different velocities, contours start at 4, step 2 K. (Bottom) 77.125 km s⁻¹, $R(^{13}\text{CO} 1 - 6 \text{ K}) / G(^{12}\text{CO} 1 - 20 \text{ K})$ / contours (20 cm; start 1.5, step 2 mJy beam⁻¹).

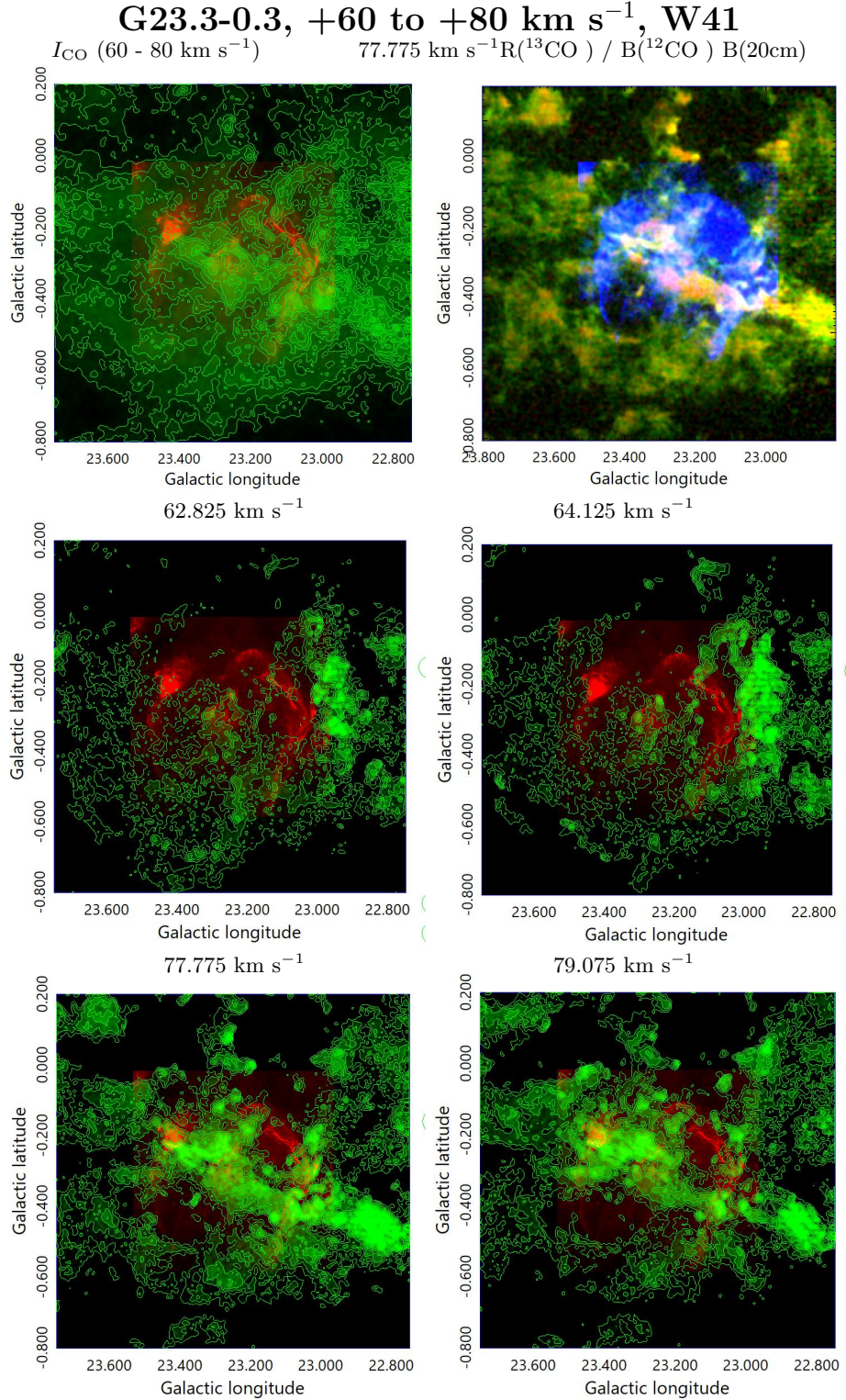


Figure 23. Same as figure 2, but for G23.3-0.3+7775 W41. (Top left) I_{CO} contours every 25 K km s⁻¹. (Top right) 77.775 km s⁻¹, R(¹³CO 0-5K) B(¹²CO 0-15K) B(20cm 1-2mJy beam⁻¹). Channel maps contours start 4K, step 1K, and 20-cm in red from 0 to 8 mJy beam⁻¹.

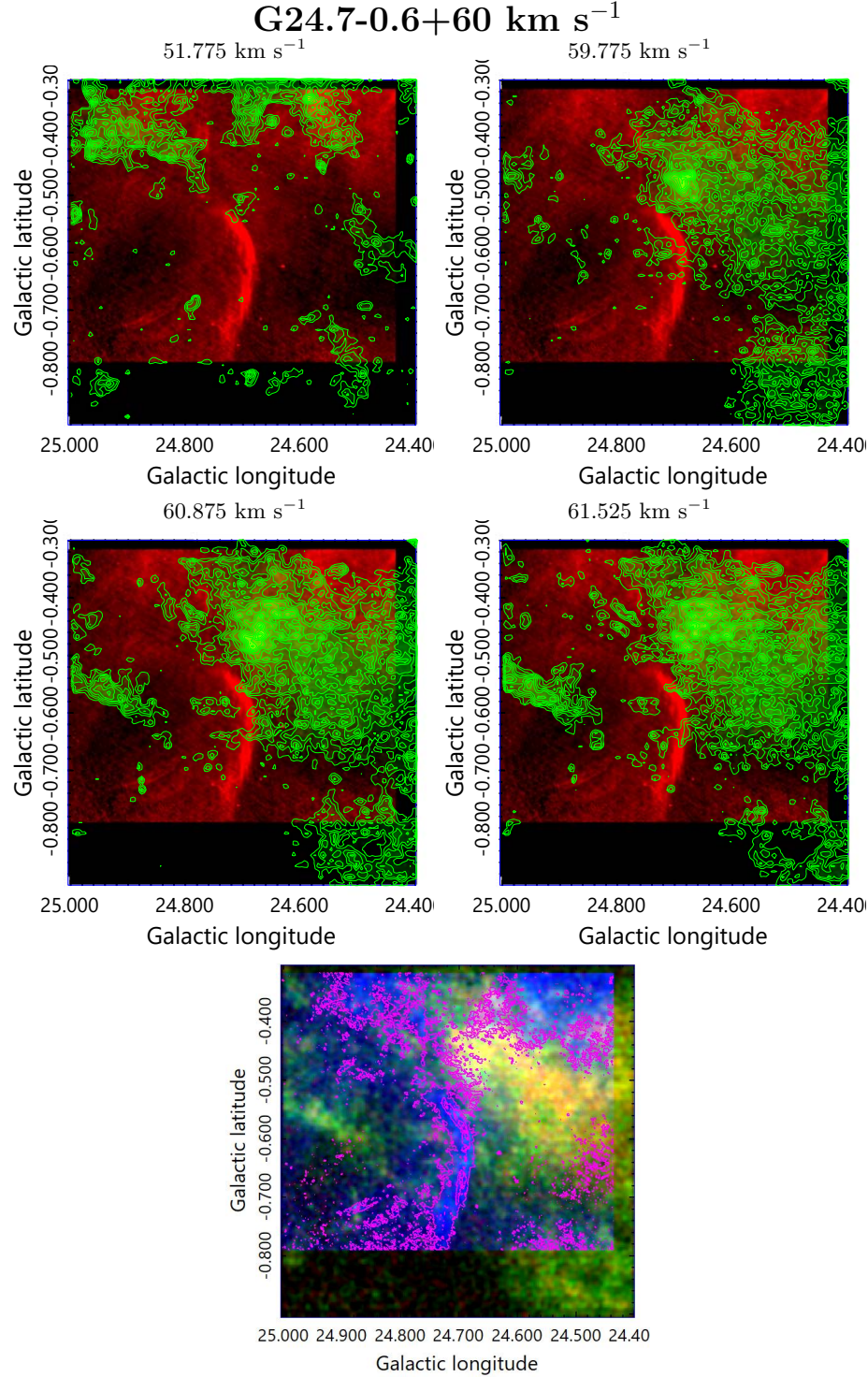


Figure 24. G24.7-0.6+60 km s⁻¹; ¹²CO (start 4K, step 1K) on 20 cm (red from 0 to 2 mJy beam⁻¹). R(¹³CO , 0, 5 K) / G(¹²CO , 0, 15 K) / 20 cm (1, 1 mJy beam⁻¹).

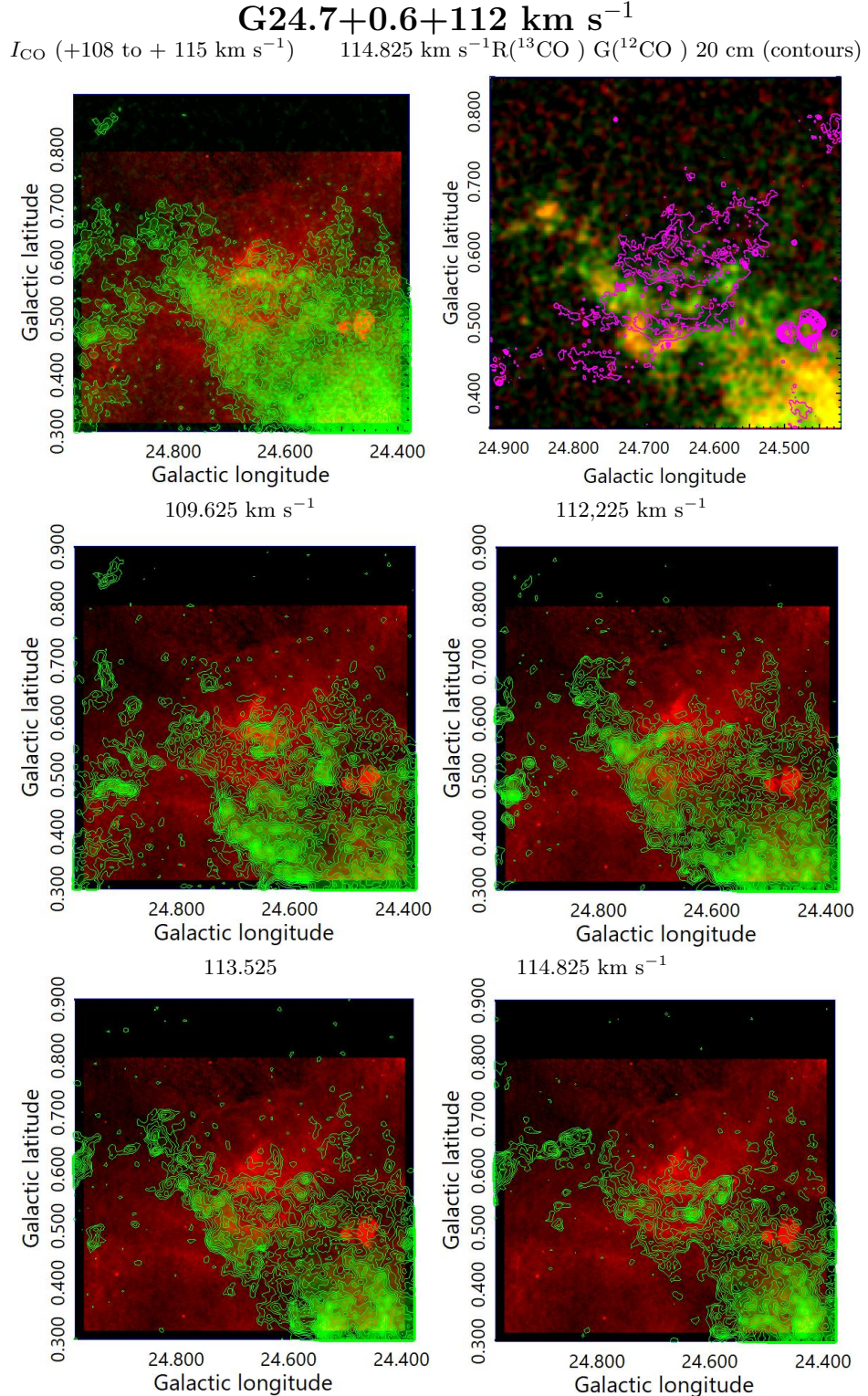


Figure 25. G24.7+0.6+112 km s⁻¹. I_{CO} (108 to 115 km s⁻¹) on 20 cm (red, auto). R (¹³CO, 0 to 3 K) / G(¹²CO, 0 to 12 K) / contours (20 cm, start 1.5, step 0.5 mJy beam⁻¹). ¹²CO (contours, start 2 K, step 1 K) on 20 cm (red from 0 to 3 mJy beam⁻¹).

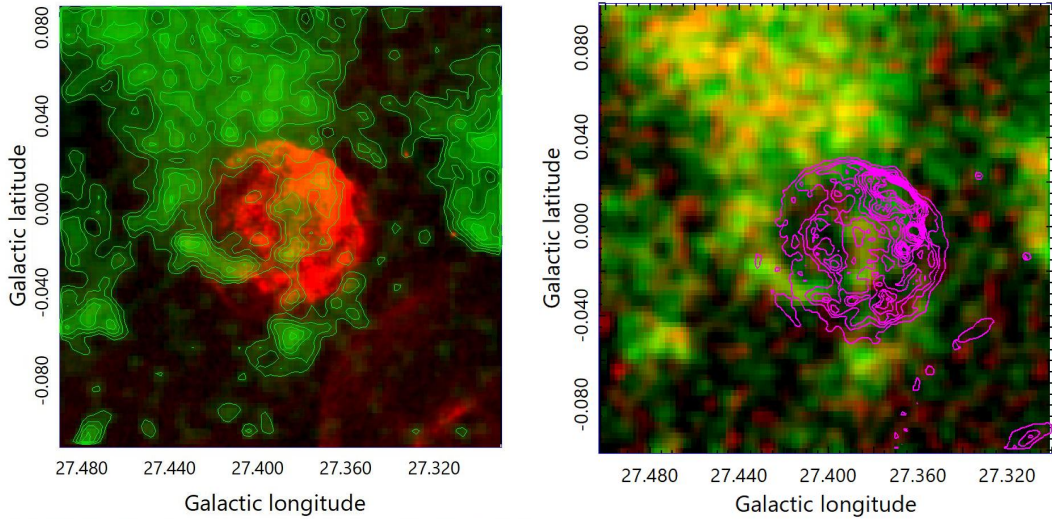
G27.4+0.0+101 km s⁻¹, 4C-04.71


Figure 26. Same as figure 2, but for G27.4, 101.175 km s⁻¹ on 20 cm continuum in red (auto). R(¹³CO , 0 to 3K) G(¹²CO , 0 to 10 K) on 20 cm (contours, start 2, step 1 mJy beam⁻¹).

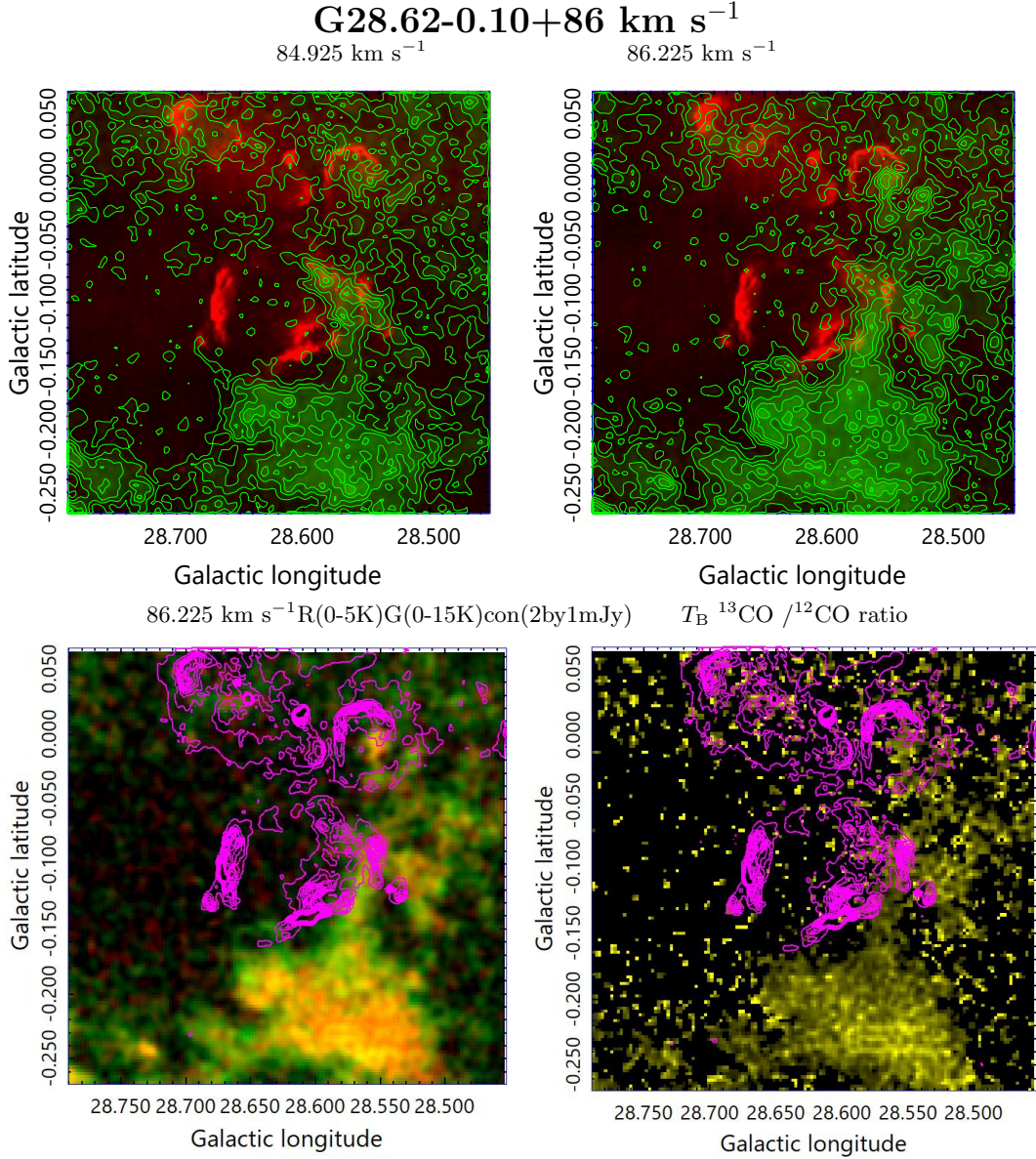


Figure 27. Same as figure 2, but for G28.62-0.10, +86 km s⁻¹. (Top) ^{12}CO contours (start 2, step 2 K) at 84.9 and 86.2 km s⁻¹superposed on 20-cm continuum (red, 0 to 8 mJy beam⁻¹). (Bottom left) R(^{13}CO , 0 to 5 K) G(^{12}CO , 0 to 15 K) on 20 cm (contours start 2, step 1 mJy beam⁻¹). (Bottom right) $^{13}\text{CO} / ^{12}\text{CO}$ T_B ratio by yellow scale superposed on the 20-cm continuum contours.

G28.62-0.10 and N49 (G28.83-0.25) at 86.225 km s^{-1}

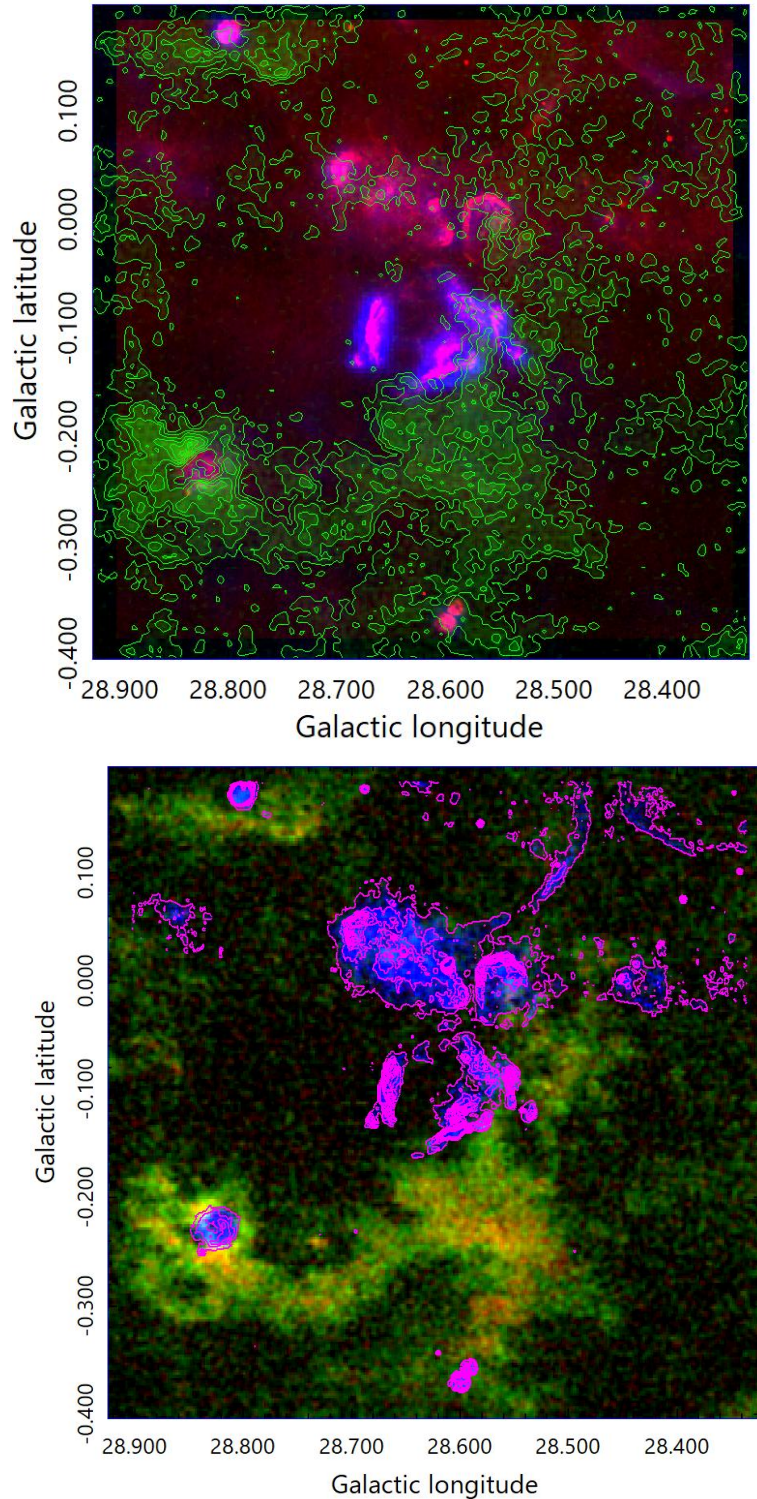


Figure 28. Same as figure C, but $^{12}\text{CO } T_B$ at 86.2 km s^{-1} for wider area including Spitzer Bubble N49 (G28.83-0.25) (Deharveng et al. 2010), showing evidence for the co-existence of the SNR and star forming region, both being embedded in the same molecular cloud.

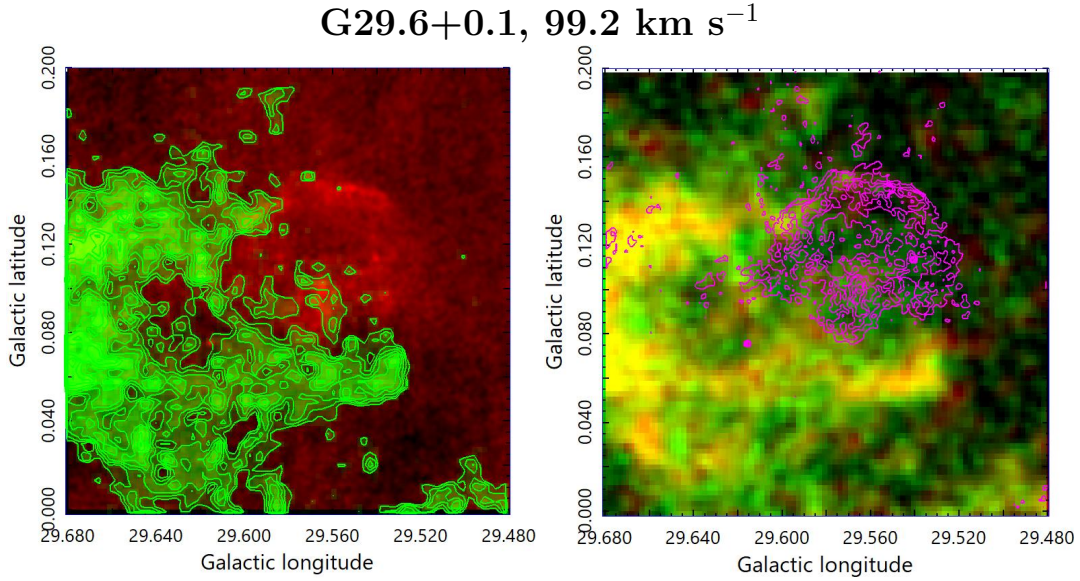


Figure 29. Same as figure 2, but for G29.6+0.1, 99.2 km s⁻¹. (Left) ^{12}CO contours (start 6 K, step 1 K) superposed on 20 cm (red). (Right) $R(^{13}\text{CO}, 0 \text{ to } 3 \text{ K}) / G(^{12}\text{CO}, 0 \text{ to } 12 \text{ K})$ contours (20 cm, start 1, step 0.2 mJy beam⁻¹)

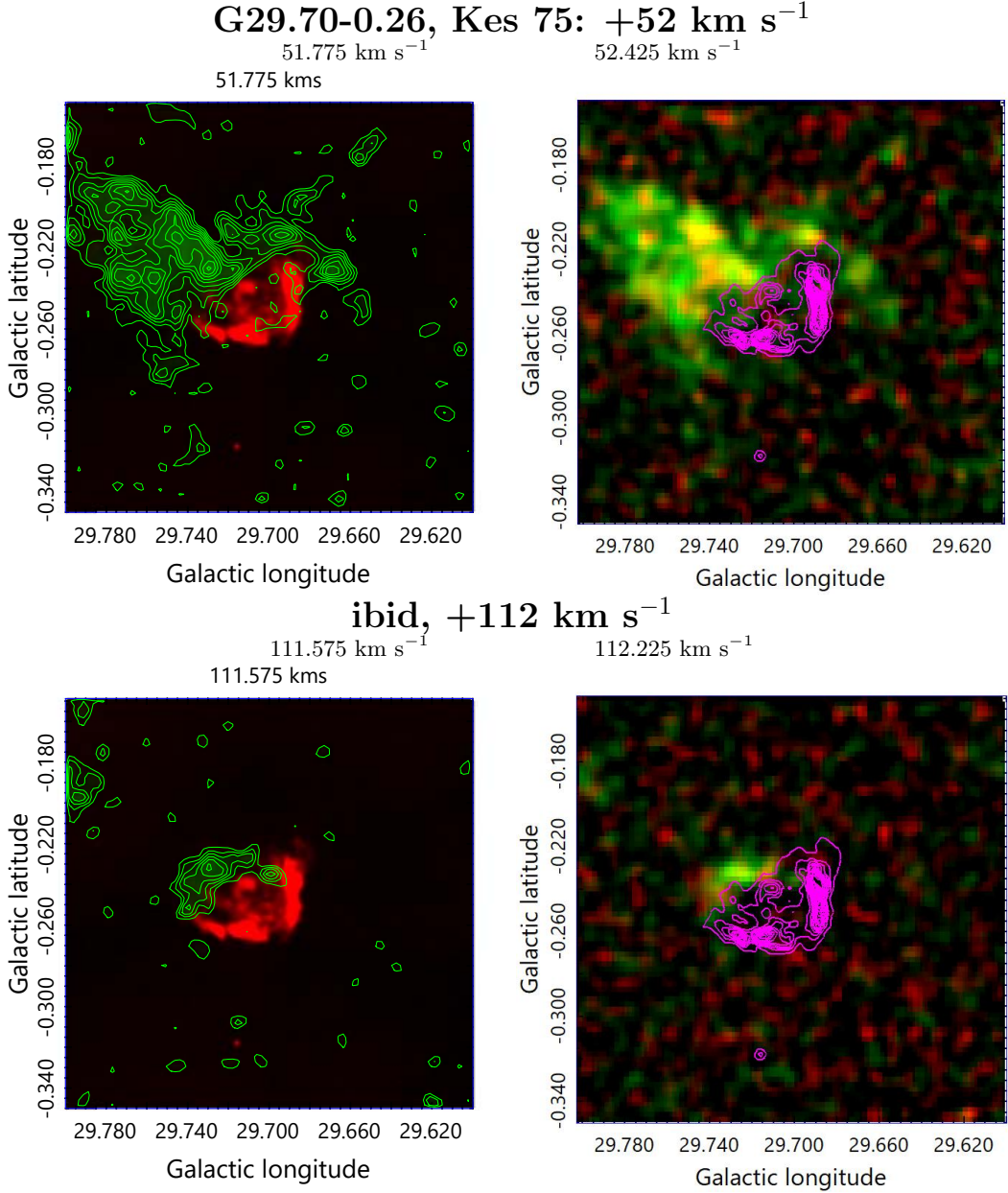


Figure 30. Same as figure 2, but for G29.70-0.26 Kes 75: 51.775 km s^{-1} or $111.575 \text{ km s}^{-1}$. (Top left) ^{12}CO contours (start 2 K, step 1 K) at $+51.775 \text{ km s}^{-1}$ superposed on 20-cm (red; 0 to 10 mJy beam $^{-1}$). (Top right) $R(^{13}\text{CO} 0 \text{ to } 3 \text{ K}) / G(^{12}\text{CO} 0 \text{ to } 10 \text{ K})$ / 20cm (contours, start 2, step 5 mJy beam $^{-1}$). (Bottom) Same, but at 112 km s^{-1} . The feature at $+52 \text{ km s}^{-1}$ is currently reported (Kilpatrick et al. 2016), but the half shell at $+112 \text{ km s}^{-1}$ is not reported.

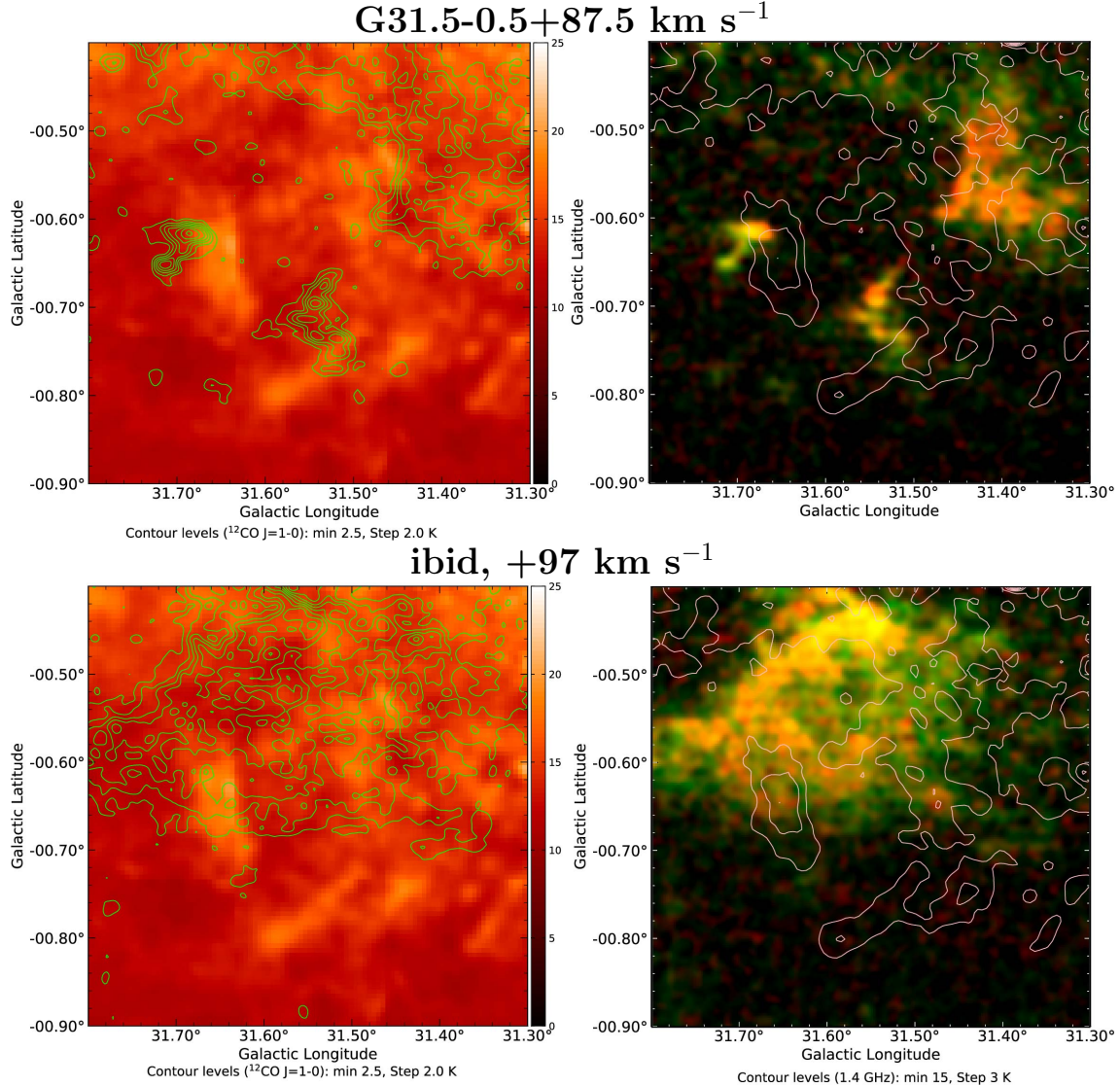


Figure 31. Same as figure 2, but for G31.5-0.5 at $+87.5 \text{ km s}^{-1}$ (top): (Left) ^{12}CO contours superposed on the radio continuum map in red. (Right) Radio continuum contours superposed on the two color composite image, red and green showing ^{12}CO and ^{13}CO $J = 1-0$ respectively. Note: From hereon, the intensity scales are indicated at the bottom of each figure. (Bottom) Same, but at $+97 \text{ km s}^{-1}$.

G31.9+0.0+107 km s⁻¹, 3C391

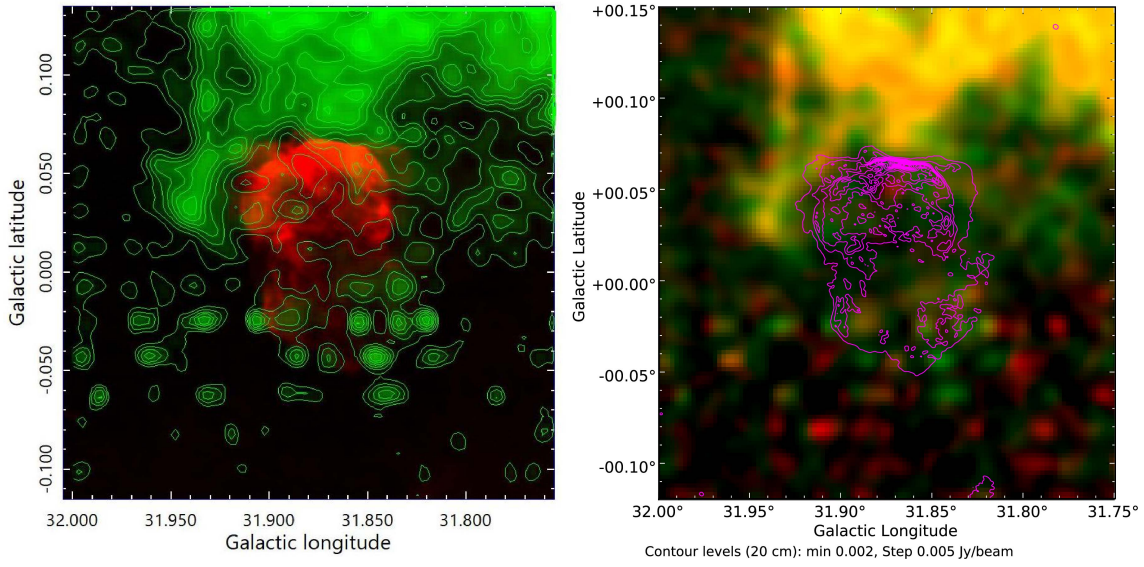


Figure 32. Same as figure 31, but for SNR G31.9+00, 107.025 km s⁻¹.

G32.1-0.9+95 km s⁻¹

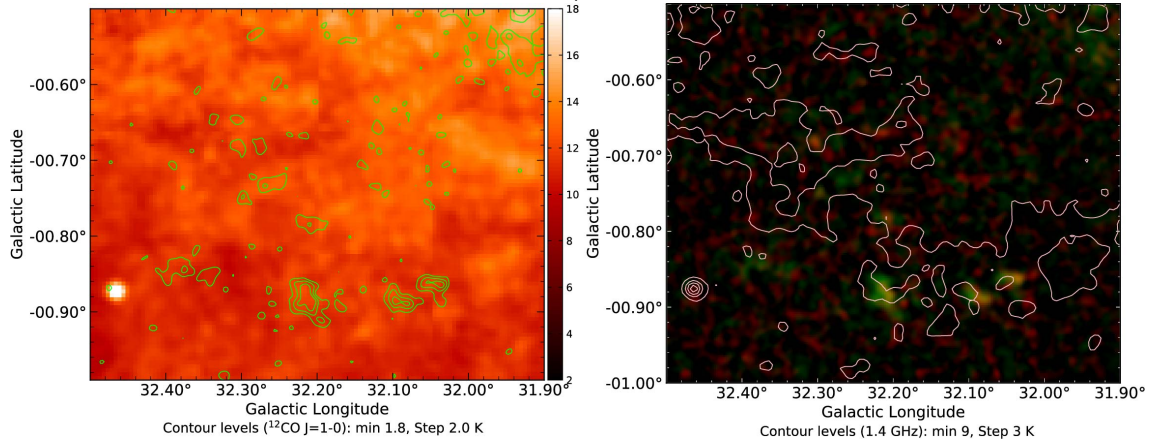


Figure 33. Same as figure 31, but for SNR G32.1-0.9+97 km s⁻¹.

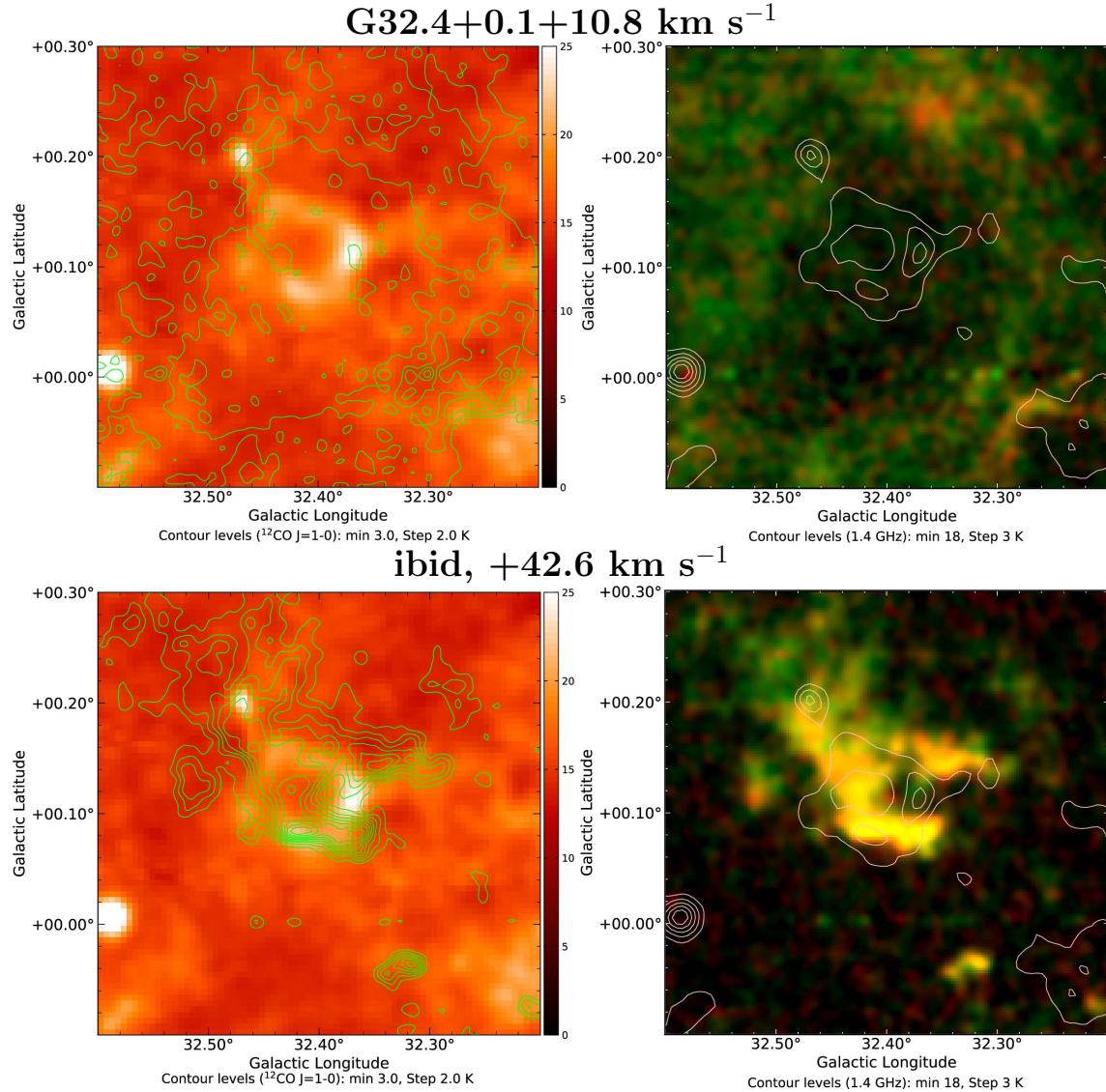
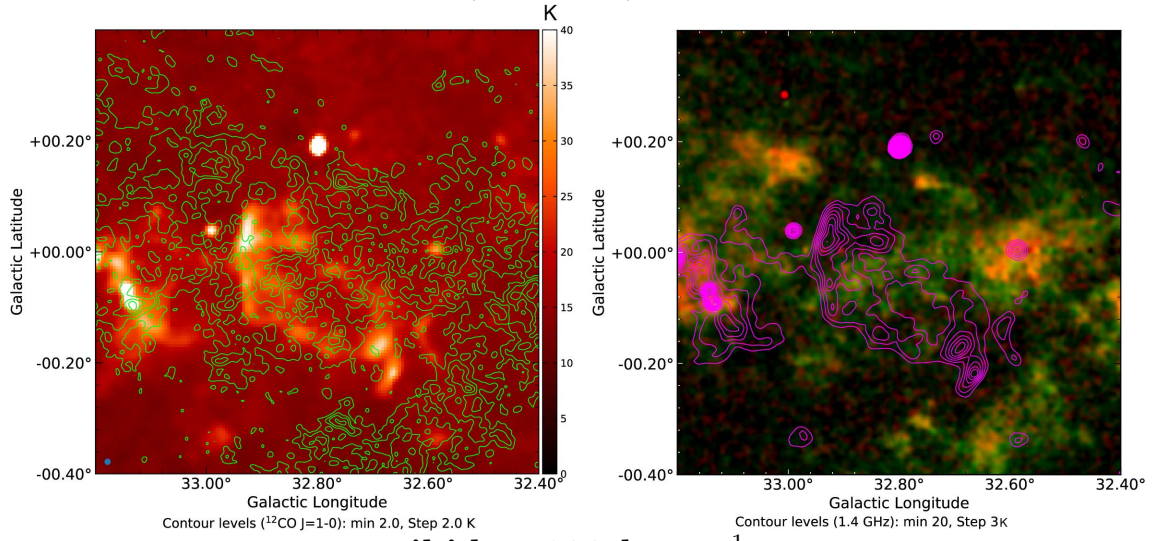


Figure 34. Same as figure 31, but for SNR G32.4+0.1 at $+10.8 \text{ km s}^{-1}$ (top), or at $+42.6 \text{ km s}^{-1}$ (bottom)

G32.8-0.1, Kes 78, $+74 \text{ km s}^{-1}$



ibid, $+103 \text{ km s}^{-1}$

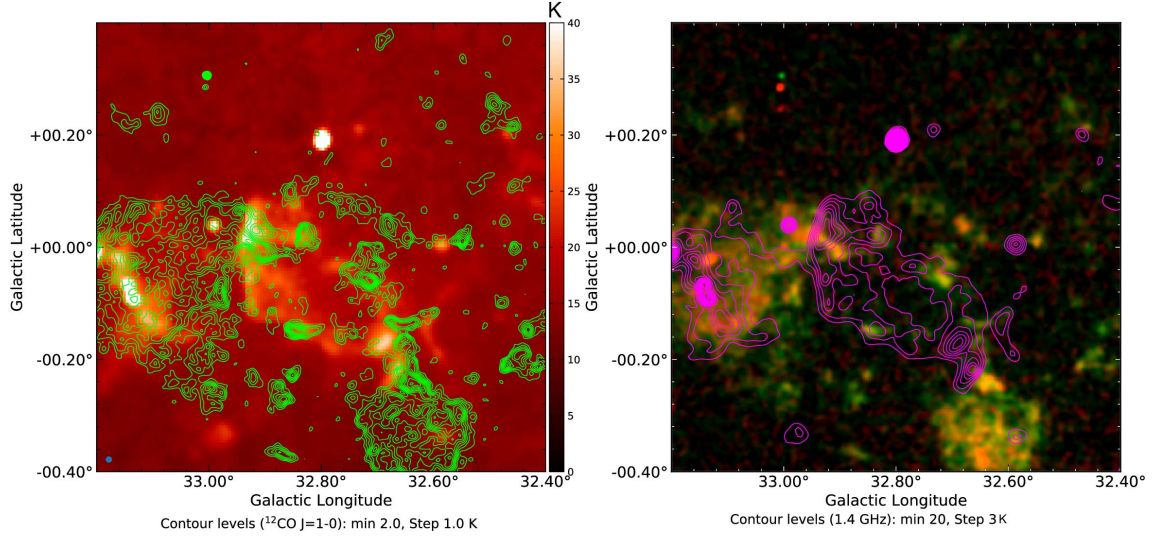


Figure 35. Same as figure 31, but for SNR G32.8-0.1 (Kes 78) at $+74 \text{ km s}^{-1}$ (top) or at $+103 \text{ km s}^{-1}$ (bottom).

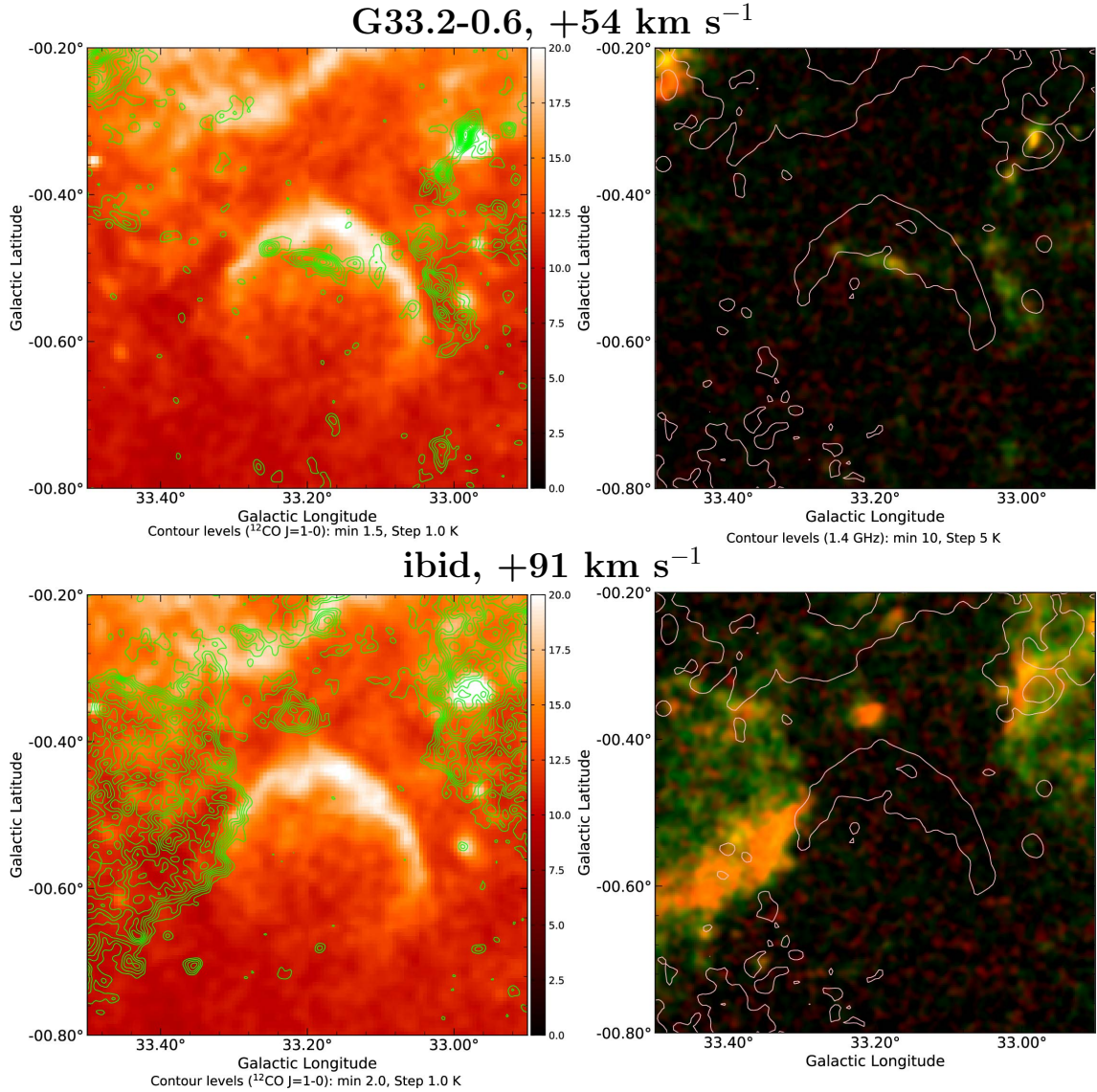


Figure 36. Same as figure 31, but for SNR G33.2-0.6 at $+54 \text{ km s}^{-1}$ (top) or at $+91 \text{ km s}^{-1}$ (bottom).

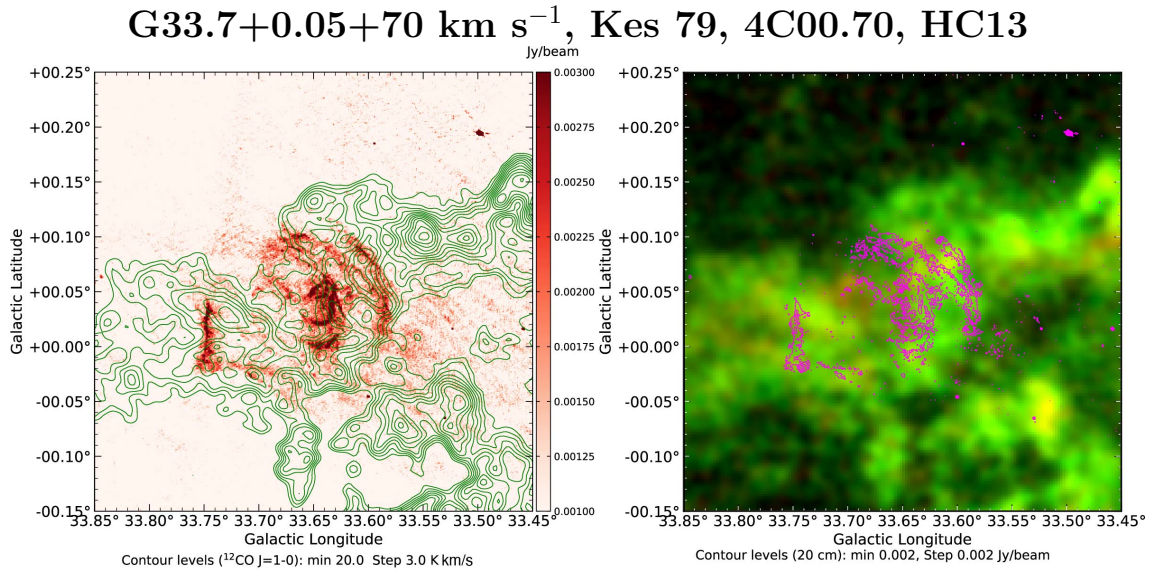


Figure 37. Same as figure 31, but for SNR G33.7+0.05+70 km s⁻¹.

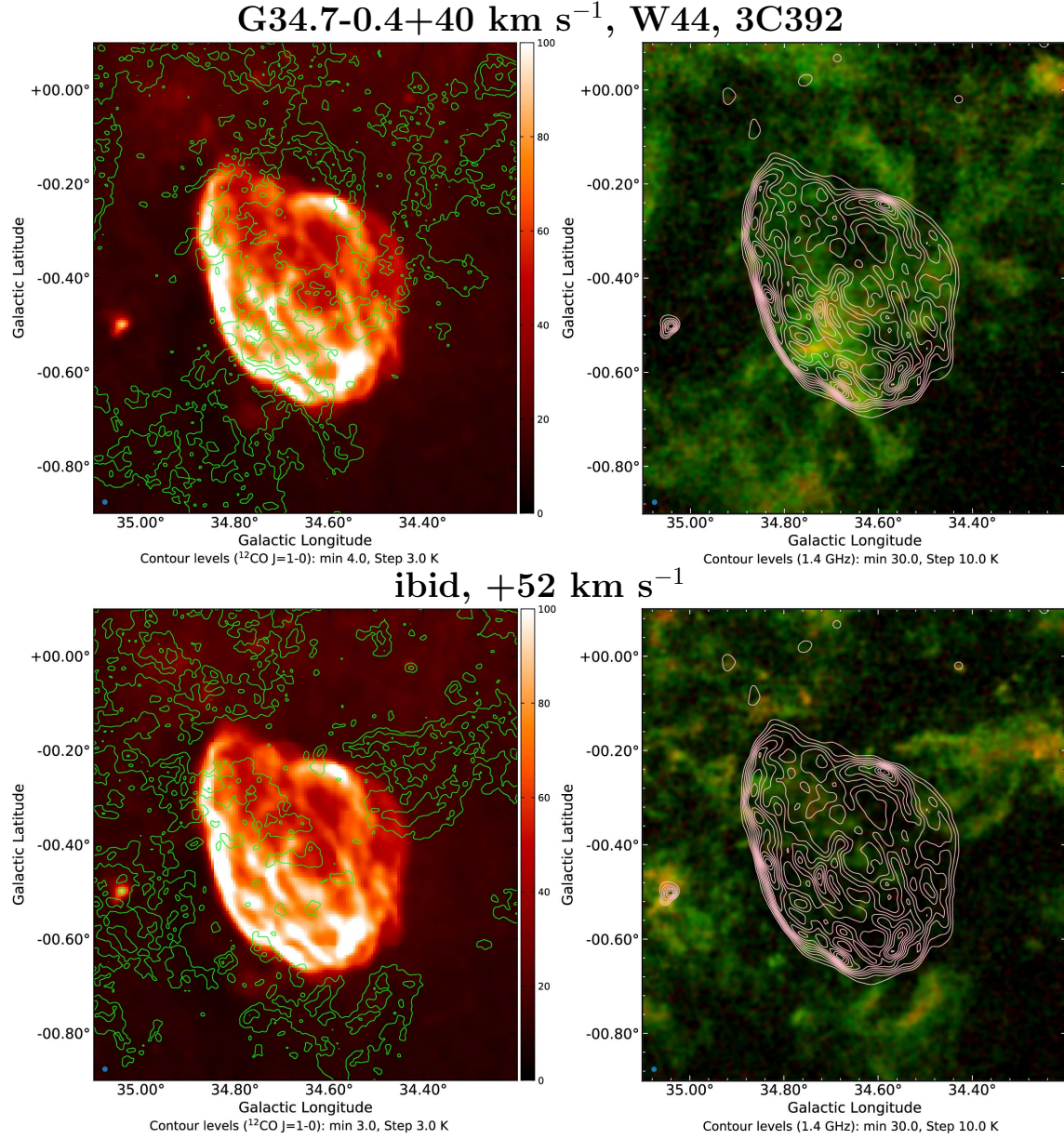


Figure 38. Same as figure 31, but for SNR G34.7-0.4+40 km s⁻¹, and +52 km s⁻¹.

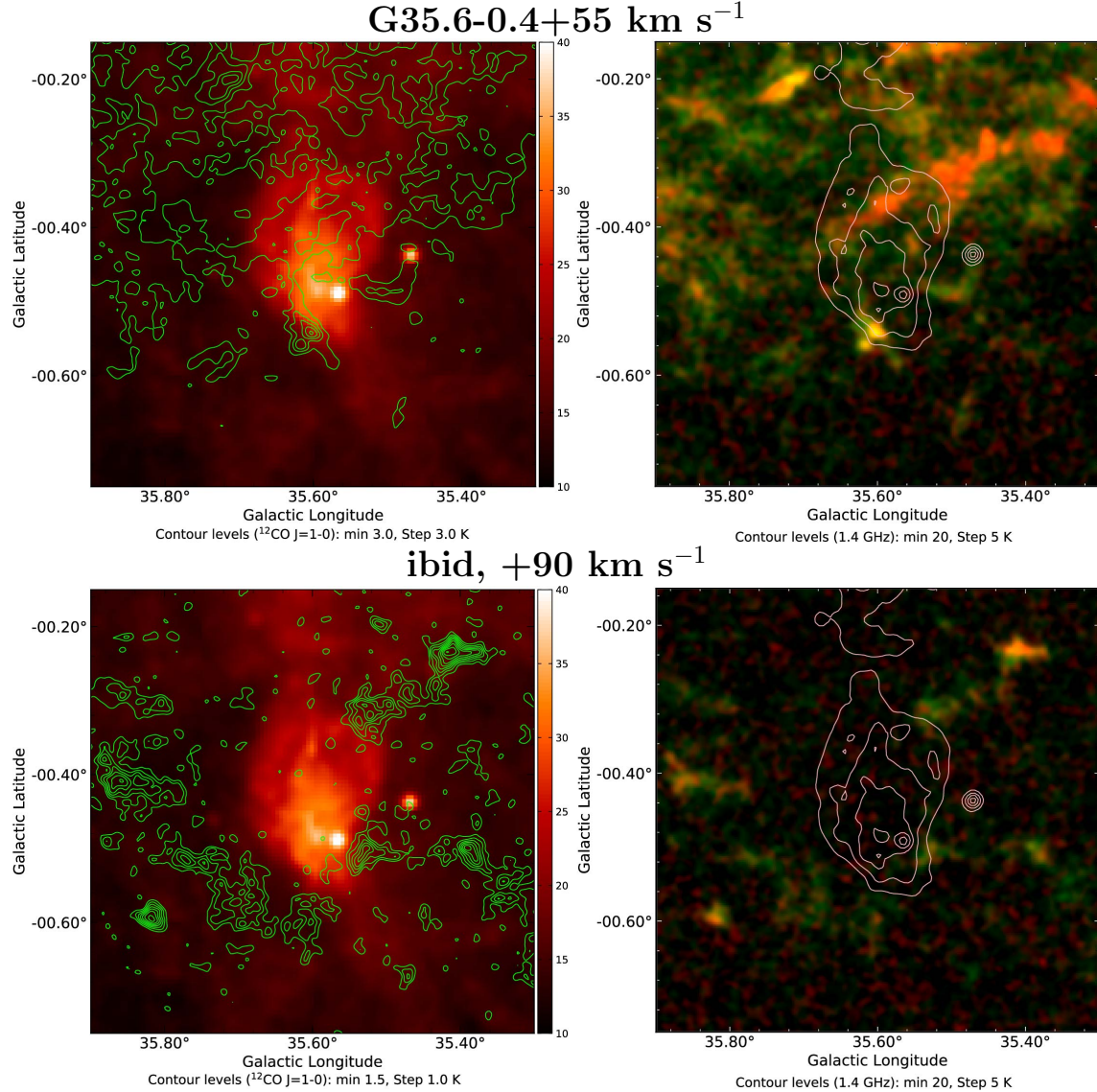


Figure 39. Same as figure 31, but for SNR G35.6-0.4, +55 and +90 km s⁻¹.

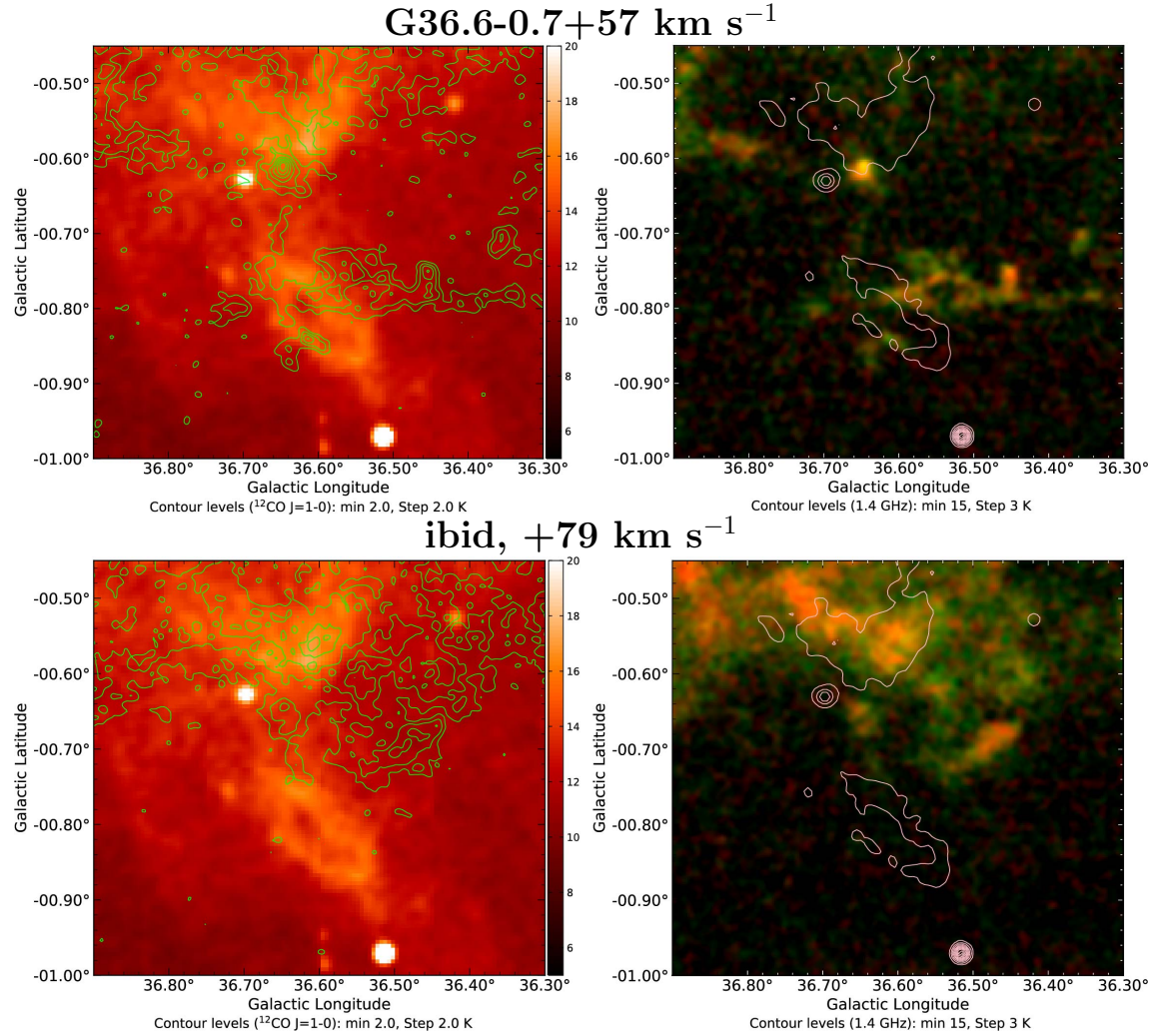
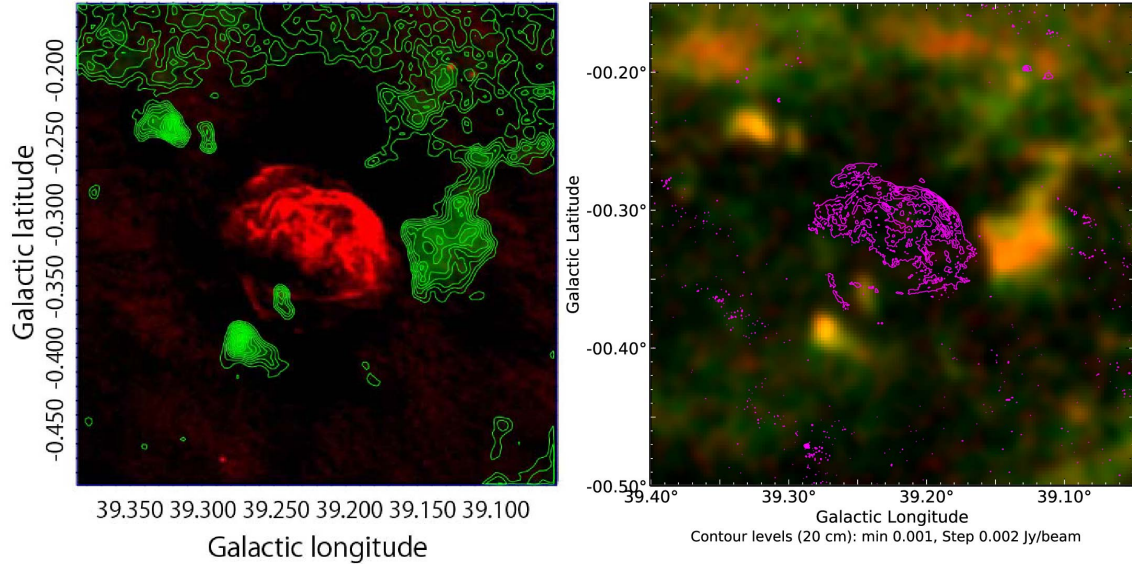


Figure 40. Same as figure 31, but for SNR G36.6-0.7 at +57 (top) or at +79 km s⁻¹(bottom).

G39.32-0.22, $+51 \text{ km s}^{-1}$ (3C396, HC24, NRAO593)



ibid, $+65 \text{ km s}^{-1}$

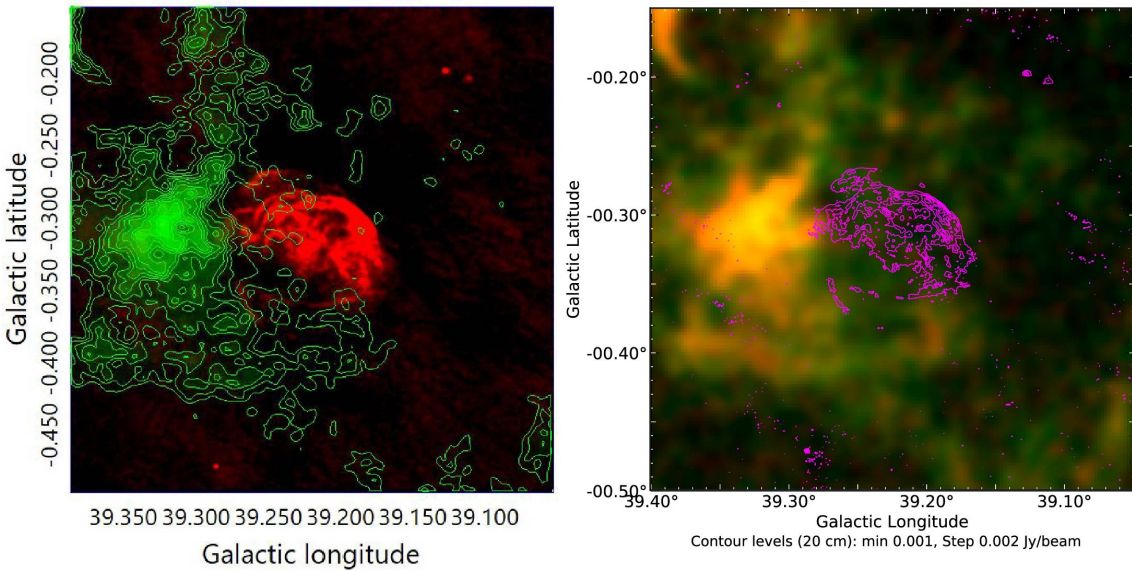


Figure 41. Same as figure 31, but for SNR G39.2-0.3, at two possible velocities, $+51$ or $+65 \text{ km s}^{-1}$.

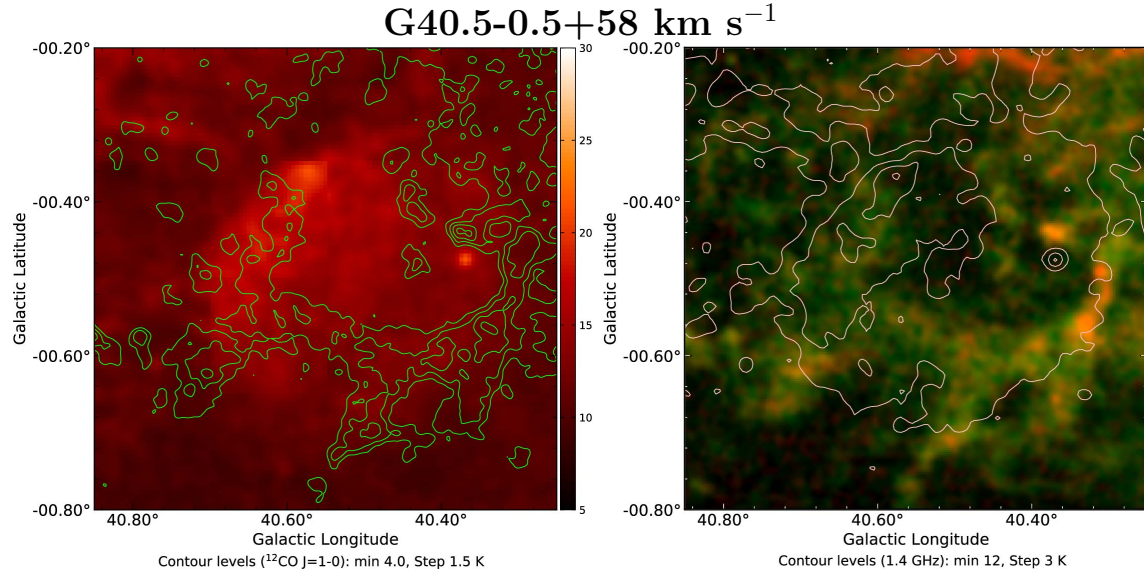


Figure 42. Same as figure 31, but for SNR G40.5-0.5+58 km s⁻¹.

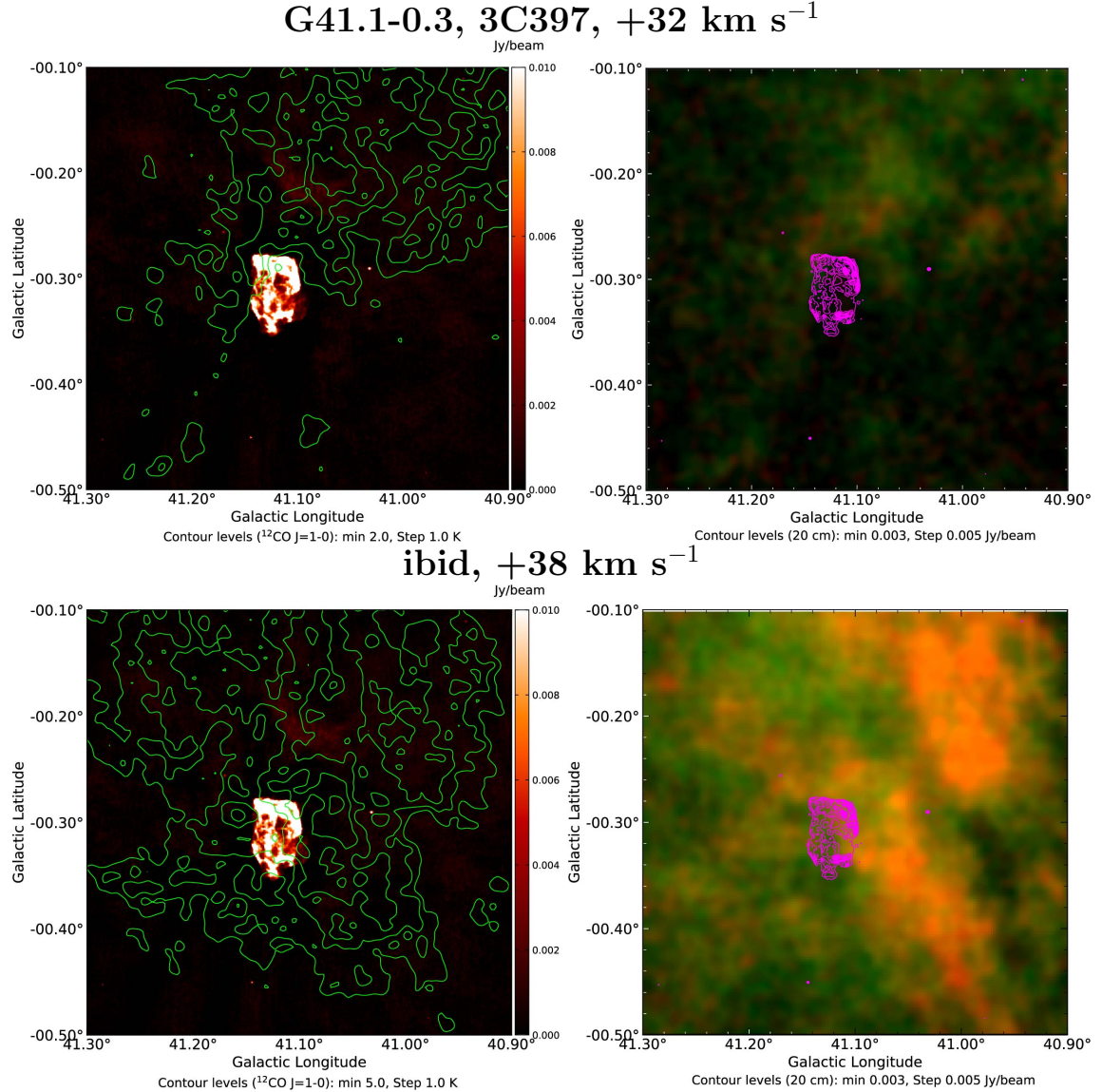


Figure 43. Same as figure 31, but for SNR G41.1-0.3, 3C 397, at $+32 \text{ km s}^{-1}$.

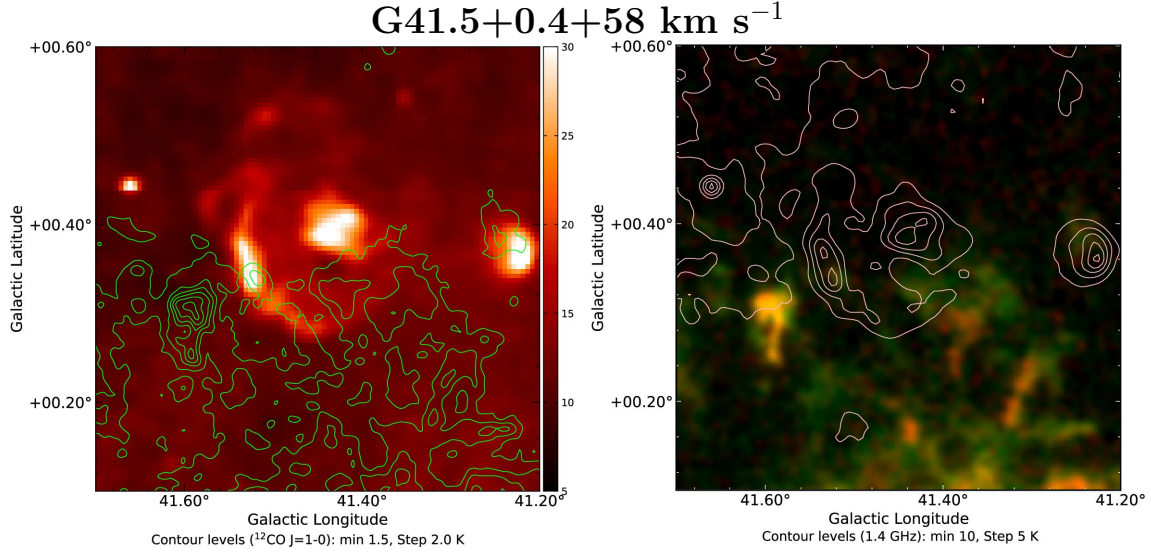


Figure 44. Same as figure 31, but for SNR G41.5+0.4+58 km s⁻¹.

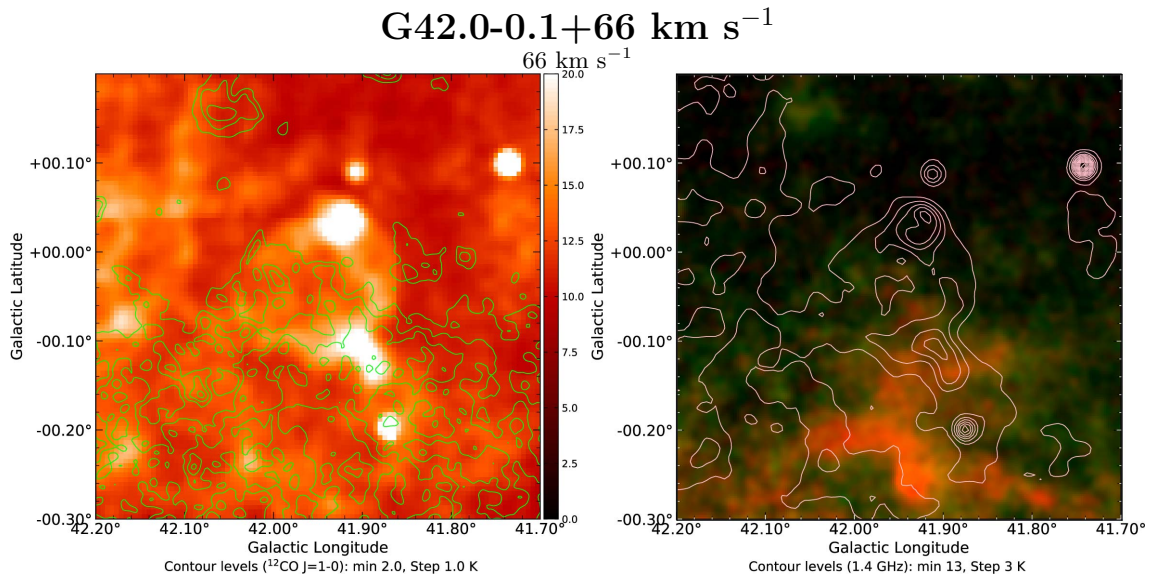


Figure 45. Same as figure 31, but for SNR G42.0-0.1+66 km s⁻¹.

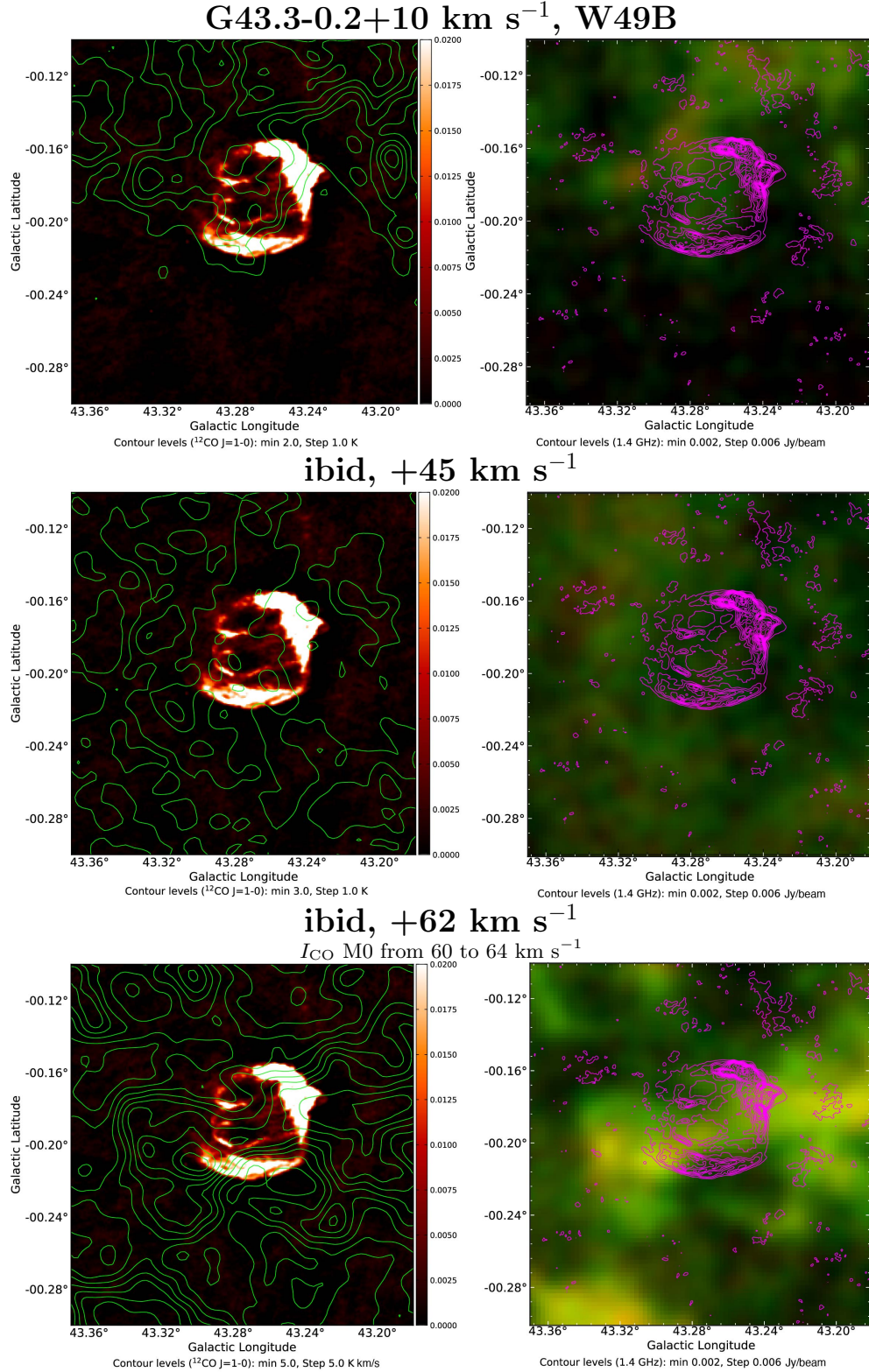


Figure 46. Same as figure 31, but for SNR G43.3-0.2+45 km s⁻¹, W49B at 10 km s⁻¹(top), 45 km s⁻¹(middle) or at 62 km s⁻¹(bottom).

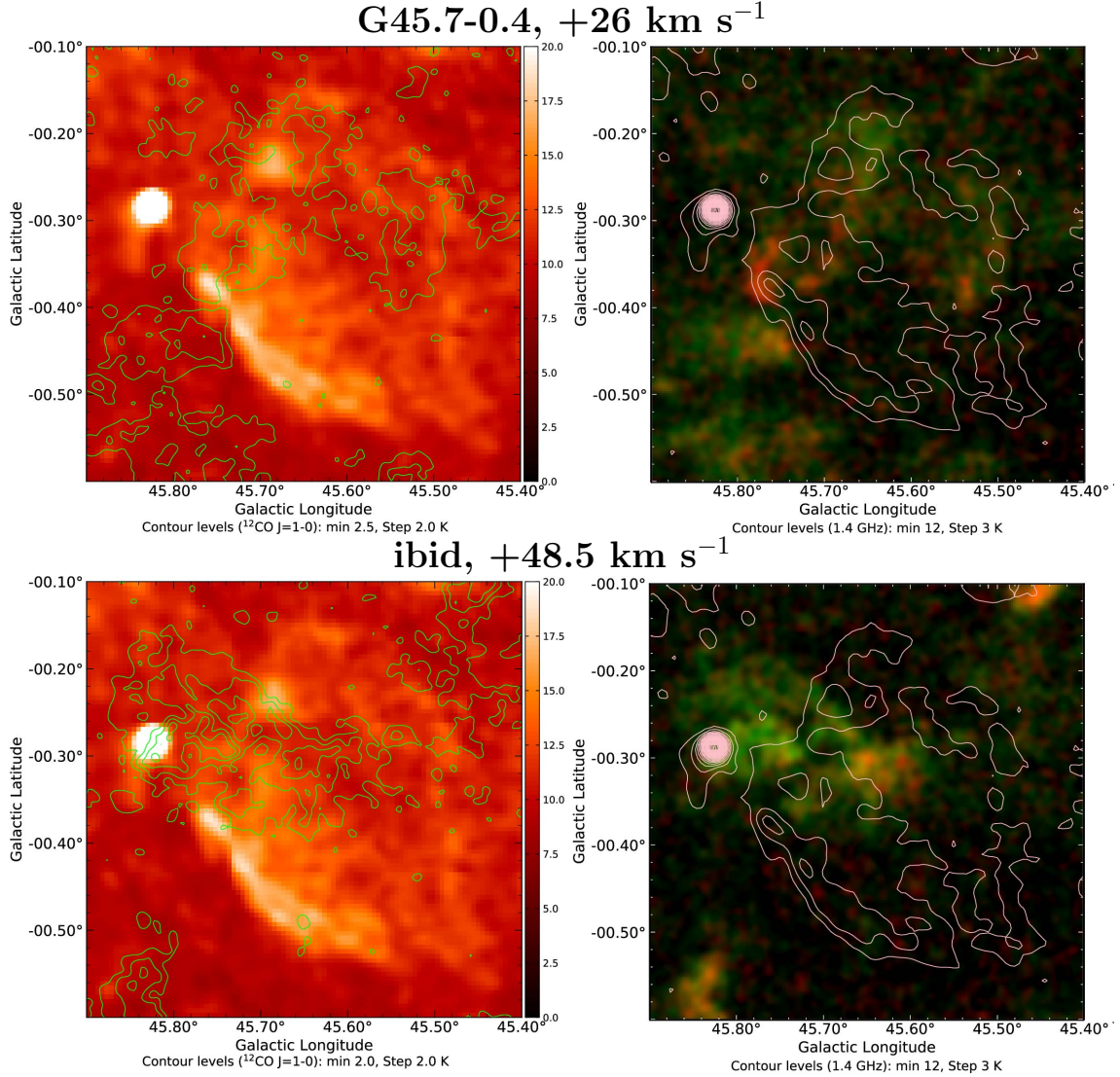


Figure 47. Same as figure 31, but for SNR G45.7-0.4 at $+26 \text{ km s}^{-1}$ (top), or at 48.5 km s^{-1} (bottom).

G46.8-0.3+52 km s⁻¹, HC30
 I_{CO} M0 from 48 to 56 km s⁻¹

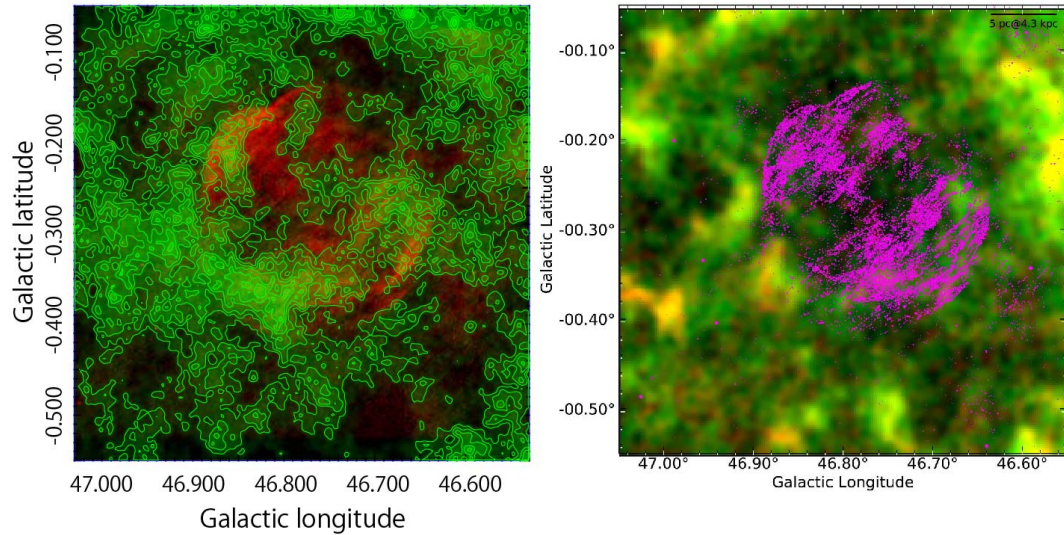


Figure 48. Same as figure 31, but for SNR G46.8-0.3; 52 km s⁻¹.

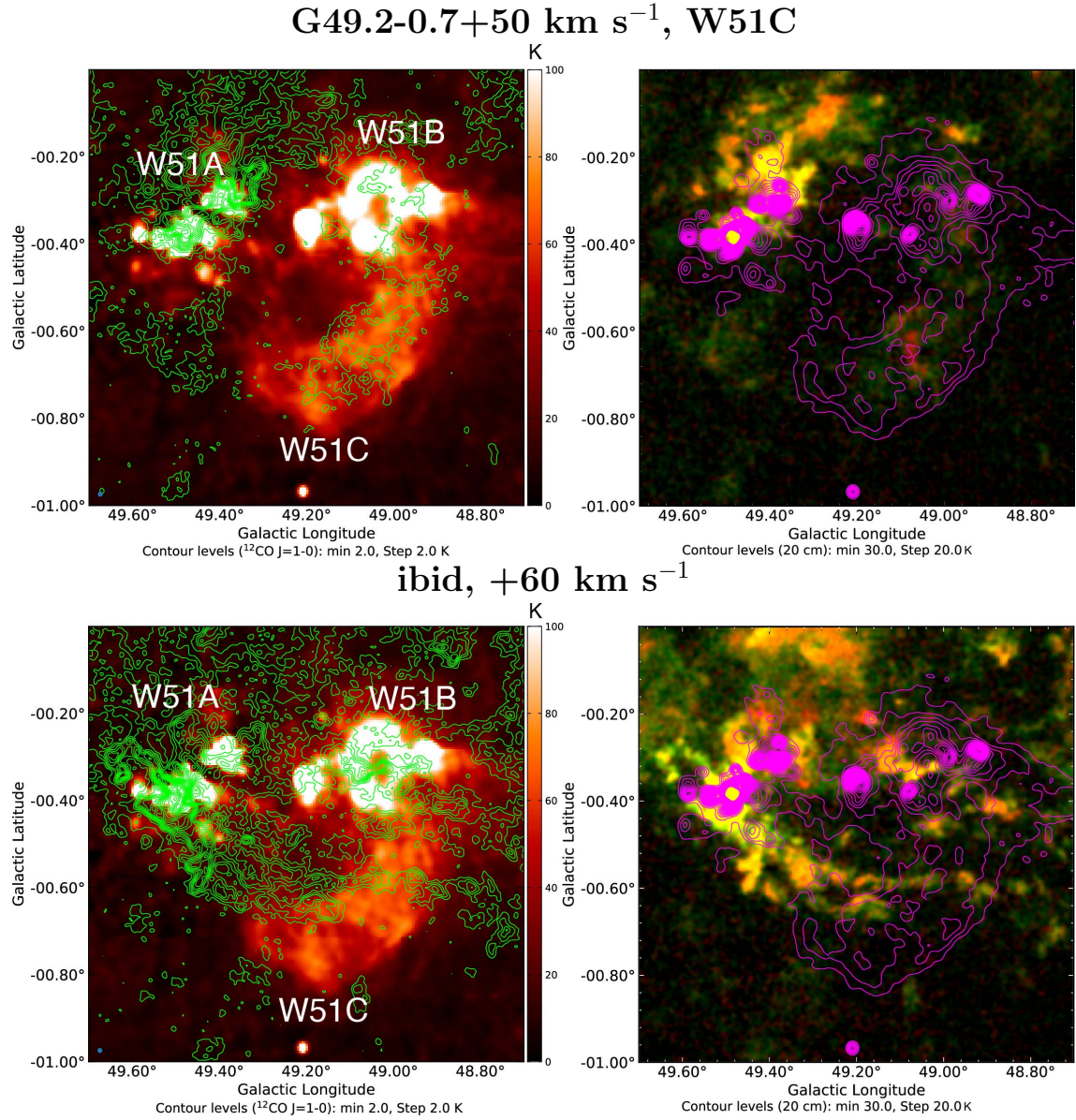


Figure 49. Same as figure 31, but for SNR G49.2-0.7; 50 and 60 km s⁻¹.

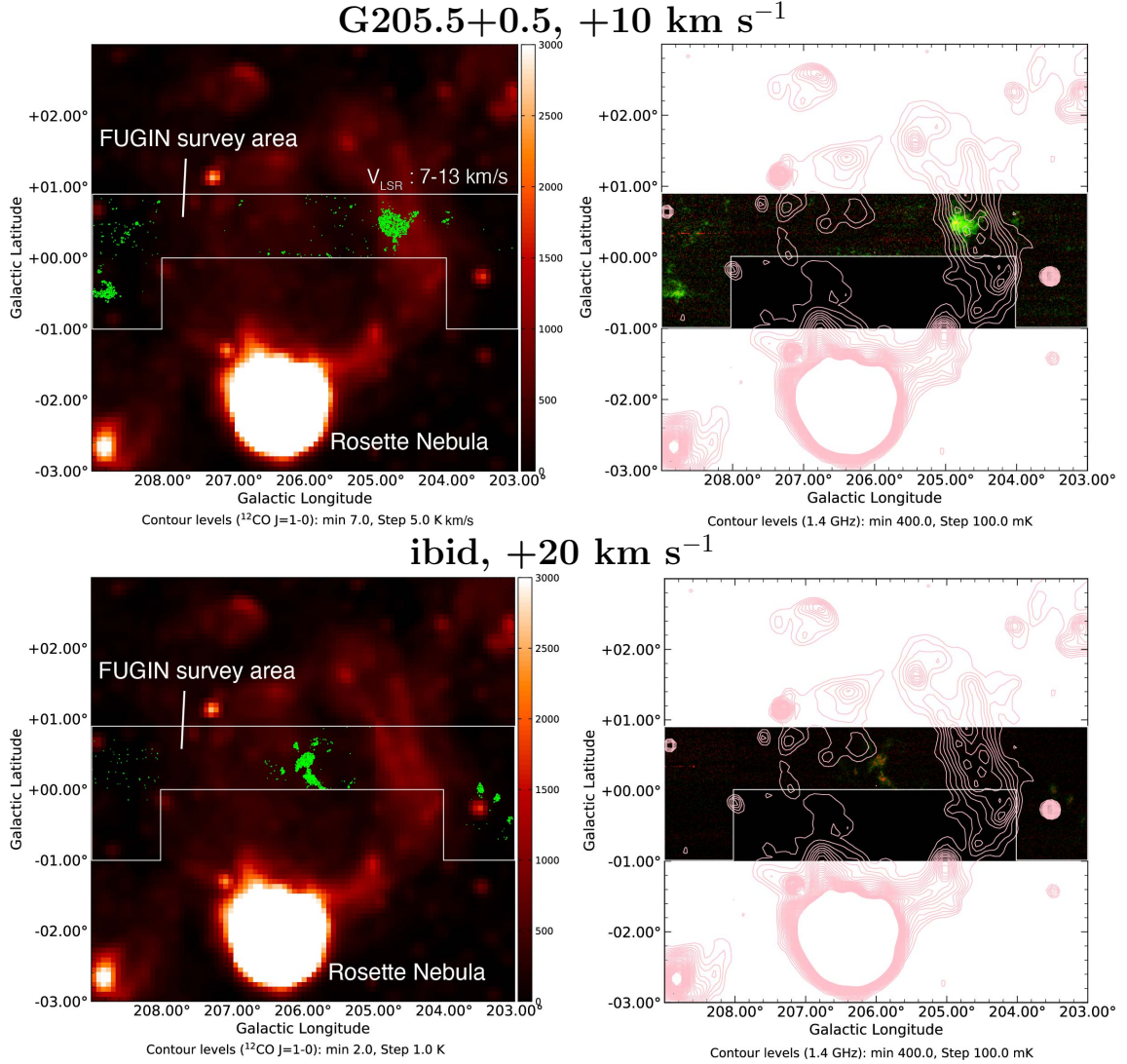


Figure 50. Same as figure 31, but for SNR G205.5+0.5, at 10 and 20 km s⁻¹. White line shows the observing area of the FUGIN CO survey. The radio continuum data is obtained by the Effelsberg 100 m telescope.

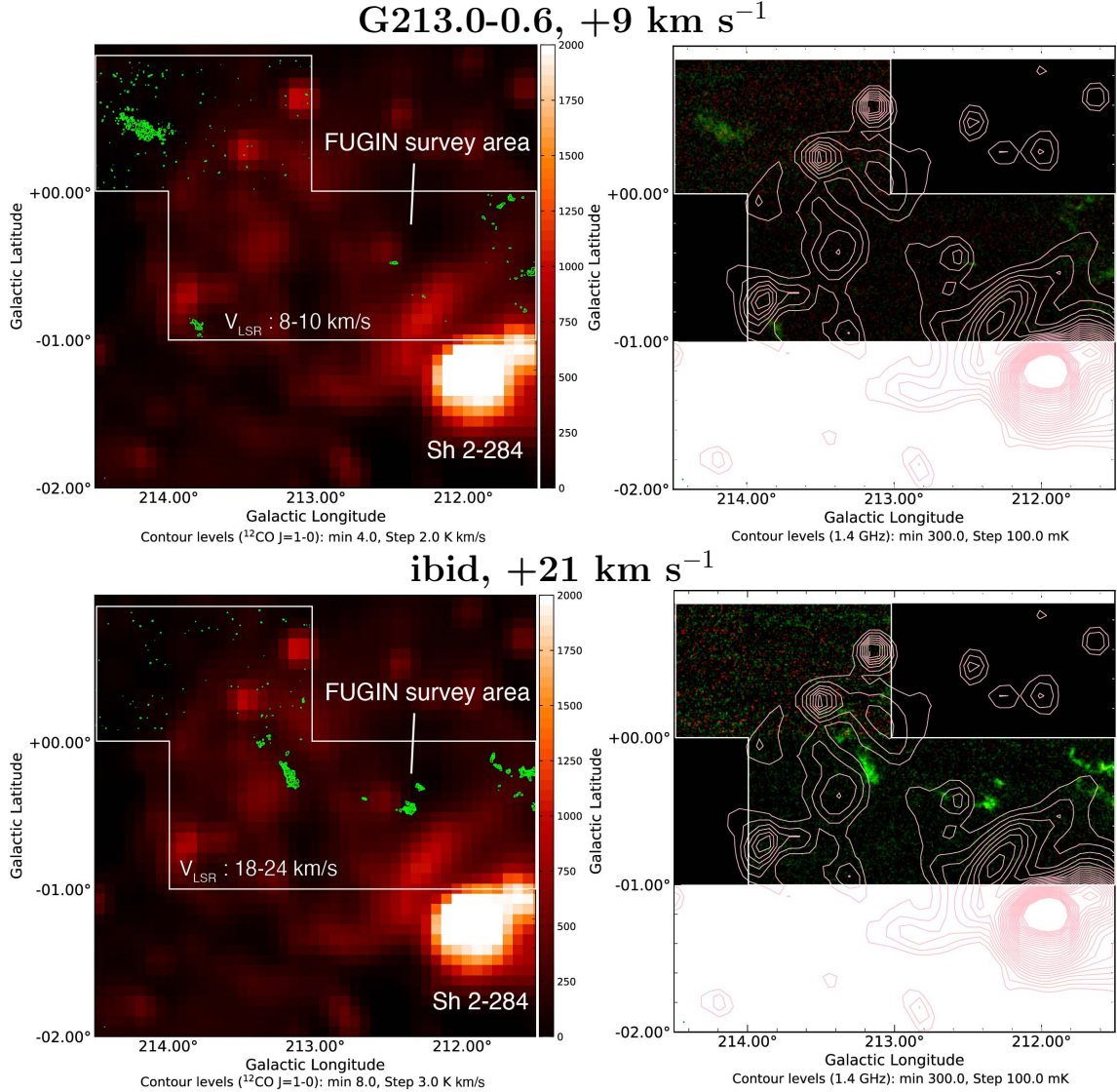


Figure 51. Same as figure 31, but for SNR G213.5-0.6; 9 and 21 km s⁻¹. White line shows the observing area of the FUGIN CO survey. The radio continuum data is obtained by the Effelsberg 100 m telescope.